Optical quantum sensing for agnostic environments via deep learning

Zeqiao Zhou,[1] Yuxuan Du,[2,3,*] Xu-Fei Yin,[4,5] Shanshan Zhao,[2] Xinmei Tian,[1,†] and Dacheng Tao[3,6,‡]

[1]*MoE Key Laboratory of Brain-inspired Intelligent Perception and Cognition, University of Science and Technology of China, Hefei 230026, China*

[2]*JD Explore Academy, Beijing 101111, China*

[3]*College of Computing and Data Science, Nanyang Technological University, Singapore 639798, Singapore*

[4]*Hefei National Research Center for Physical Sciences at the Microscale and School of Physical Sciences, University of Science and Technology of China, Hefei 230026, China*

[5]*CAS Center for Excellence in Quantum Information and Quantum Physics, University of Science and Technology of China, Shanghai 201315, China*

[6]*School of Computer Science, The University of Sydney, NSW 2008, Australia*

(Received 9 August 2024; accepted 25 November 2024; published 12 December 2024)

Optical quantum sensing promises measurement precision beyond classical sensors termed the Heisenberg limit (HL). However, conventional methodologies often rely on prior knowledge of the target system to achieve HL, presenting challenges in practical applications. Addressing this limitation, we introduce an innovative deep-learning-based quantum sensing scheme (DQS), enabling optical quantum sensors to attain HL in agnostic environments. DQS incorporates two essential components: a graph neural network (GNN) predictor and a trigonometric interpolation algorithm. Operating within a data-driven paradigm, DQS utilizes the GNN predictor, trained on offline data, to unveil the intrinsic relationships between the optical setups employed in preparing the probe state and the resulting quantum Fisher information (QFI) after interaction with the agnostic environment. This distilled knowledge facilitates the identification of optimal optical setups associated with maximal QFI. Subsequently, DQS employs a trigonometric interpolation algorithm to recover the unknown parameter estimates for the identified optical setups. Extensive experiments are conducted to investigate the performance of DQS under different settings up to eight photons. Our findings not only offer a different lens through which to accelerate optical quantum sensing tasks but also catalyze future research integrating deep learning and quantum mechanics.

DOI: 10.1103/PhysRevResearch.6.043267

I. INTRODUCTION

Quantum sensing, by measuring physical quantities with a precision approaching Heisenberg limit (HL), has emerged as a leading practical application of quantum technology [1,2], which offers new opportunities in various fields, including medicine, navigation, optical time transfer, and energy detection [3–6]. Achieving the HL demands a quantum sensing scheme meticulously tailored to the target quantity, encompassing optimal probe preparation and parameter estimation [7,8]. Linear optics, given its robustness against noise and decoherence combined with its long-range communication capability, stands out as a premier platform for quantum sensing [9]. Nevertheless, in practical scenarios where the quantum system is unknown or uncontrolled [10,11], conventional methods become infeasible, as they typically depend on explicit knowledge of system to devise optimal schemes, while such direct information is often unavailable from interactions with target environments [12–14]. Thus, despite promising precision enhancements offered by optical quantum sensing, designing an optimal scheme for agnostic environments remains a largely unexplored challenge.

Conventional optical quantum sensing schemes require a known expression of the target environment. This allows for the exact derivation of the optimal probe state and the design of the corresponding observable or estimator using methods like maximum likelihood [7,8]. Classical computer algorithms are then used to determine the optical setup needed to prepare such a quantum state. One main category is direct simulation methods [15–18]. However, simulating quantum processes of it remains costly due to the exponential complexity relative to the size of the quantum system. Similar approach involves reinforcement learning algorithms [19–24]. For example, the optical setup is treated as a series of actions performed by an agent within an environment [21]. This agent adjusts its actions based on active learning methods, guided by feedback in the form of researcher-designed rewards. However, these algorithms require either full characterization of the target

*Contact author: duyuxuan123@gmail.com
†Contact author: xinmei@ustc.edu.cn
‡Contact author: dacheng.tao@ntu.edu.sg

environment to simulate on classical computers or expensive continuous interactions with the environment, which may not be feasible in agnostic environmental settings.

Variational quantum algorithms have emerged as a promising method for directly preparing probe states on parametrized quantum circuits [25,26]. By fixing the layout of the quantum ansatz, the gate parameters are optimized concerning a target function, approximating the optimal probe state. However, since most optical devices lack parameters, conducting optimization on an optical platform is challenging. Recent efforts have been made to apply similar techniques on optical platforms [27,28]. Specifically, a parametrized fully connected graph corresponding to a quantum state is optimized via gradient descent. After optimization, the graph is mapped to an optical setup. Yet, this approach still assumes a known target state to define the target function [27].

Deep learning has recently been demonstrated as a powerful tool to learn quantum systems with partial or incomplete information [29]. Initial works have focused on efficiently learning quantum systems from local measurement results, reconstructing the quantum state with various architectures of neural networks [30–33]. These efforts further extend to the quantification of essential properties in quantum systems, such as entanglement [34–36] or fidelity [37–39]. Concurrently, other works have focused on learning interpretable representations for quantum systems [40] or quantum experiments [41,42], discovering novel insights from unlabeled data via a data-driven paradigm. Recently, deep learning has also been employed to design quantum circuits for various quantum algorithms, such as the variational quantum eigensolver and quantum kernel methods [43,44]. With the continuous advancement of both algorithmic frameworks and hardware infrastructures, deep learning holds the appealing potential to facilitate optical quantum sensing in realistic applications.

In this work, we propose a high-level algorithmic framework called deep-learning-based quantum sensing (DQS), designed to enhance optical quantum sensing in agnostic environments. DQS is a flexible scheme that integrates deep learning to process partial information from environmental interactions and other advanced subroutines to identify the optimal configuration by maximizing the quantum Fisher information (QFI) of the probe state, the intrinsic determinant of sensing precision. To achieve this, DQS employs a graph neural network (GNN) to learn the mapping rule between the optical setups and the corresponding QFI from a few offline data. The trained GNN efficiently searches for the optical configuration with the highest QFI among explored candidates. Once the optimal optical setup for probe preparation is identified, DQS integrates a postprocessing method to estimate the target parameter from the measurement results of the probe state in agnostic settings. In numerical experiments, through evaluating the DQS on data sets with different sizes and numbers of photons, we observe that DQS can perform well with a relatively small amount of training examples, and even discover the optimal probes when not encountering them during training. Furthermore, DQS saturates HL in an eight-photon quantum sensing task, while a trivially designed scheme fails. Our proposal can be readily adapted to other relevant optical tasks, opening up exciting prospects for future research on quantum technology applications in realistic settings.

II. PRELIMINARY

A. Optical quantum computing

We discuss qubits that are encoded through photon polarization. Specifically, the state $|0\rangle$ corresponds to vertically polarized light, while $|1\rangle$ relates to horizontally polarized light. In this representation, an n-qubit quantum state (or, equivalently, an n-photon state) can be written as

$$|\psi\rangle = \sum_{i\in\{0,1\}^n} \alpha_i |i\rangle. \tag{1}$$

Compared to other quantum platforms, optical quantum computing has some unique phenomena, such as the HOM effect. This effect causes several photons to occupy the same path, making them indistinguishable, and effectively reducing them to a single-qubit state. We use postprocessing to ensure that an n-qubit state remains a superposition of n-qubit bases. For instance, when two photons are equally likely to be in one path or to split between two paths, the state is represented as $|\psi\rangle = |0_a 0_b\rangle + |0_a^2\rangle$ (where the superscript 2 indicates two indistinguishable photons in path a). Postprocessing then simplifies this state to $|\psi\rangle = |0_a 0_b\rangle$.

For the optical quantum sensing, we confine the probe state's preparation to a sequence derived from a linear optical toolbox encompassing spontaneous parametric down-conversion (DC), beam splitter (BS), polarized beam splitter (PBS), half-wave plate (HWP), quarter-wave plate (QWP), and mirror reflection (R) (refer to Appendix A for detailed definition). Moreover, without loss of generality, we distinguish devices applying on different photon paths or with different parameters. Given the connectivity and noise constraints, the sequence's length is limited.

Initial quantum states are produced via a process known as spontaneous parametric down-conversion. For instance, applying DC on paths "a" and "b" can produce states such as $|0_a 0_b\rangle$, $|1_a 1_b\rangle$, or a superposition $|0_a 0_b\rangle + |1_a 1_b\rangle$. To generate a multiqubit initial state, one can use multiple DC processes. For example, to get a four-qubit initial state, one might produce $|0_a 0_b\rangle \otimes |1_c 1_d\rangle$. Once the initial state is produced using DC, various devices act on it to prepare the desired quantum state.

In Fig. 1, we show how a quantum state is generated with an optical setup. Starting with two DC to preparing the initial state, the sequence "$\mathrm{R}_b \to \mathrm{PBS}_{b,c} \to \mathrm{R}_c$" is applied on it. The state is $i|0_a 0_b 1_b 1_d\rangle - |0_a 0_b 0_c 0_d\rangle - |1_a 1_b 1_c 1_d\rangle - i|1_a 0_c 1_c 0_d\rangle$. After postprocessing to filter out the invalid basis, the state is $-|0_a 0_b 0_c 0_d\rangle - |1_a 1_b 1_c 1_d\rangle$, which is a GHZ state.

B. Optical quantum sensing

Here we consider single-parameter linear optical quantum sensing in real-world scenarios. As shown in Fig. 2(a), the process begins with an initial state ρ_{in}. The implementation of an optical setup acts as an encoding channel $\mathrm{E}_{\mathrm{enc}}$ to prepare an N-qubit probe state $\rho = \mathrm{E}_{\mathrm{enc}}(\rho_{\mathrm{in}})$ where $\rho_{\mathrm{in}}, \rho \in \mathbb{C}^{2^N \times 2^N}$. Subsequently, this probe state interacts with the environment via a channel given by

$$S_\theta(\rho) = e^{-\frac{1}{2}i\theta H} \rho e^{\frac{1}{2}i\theta H}, \tag{2}$$

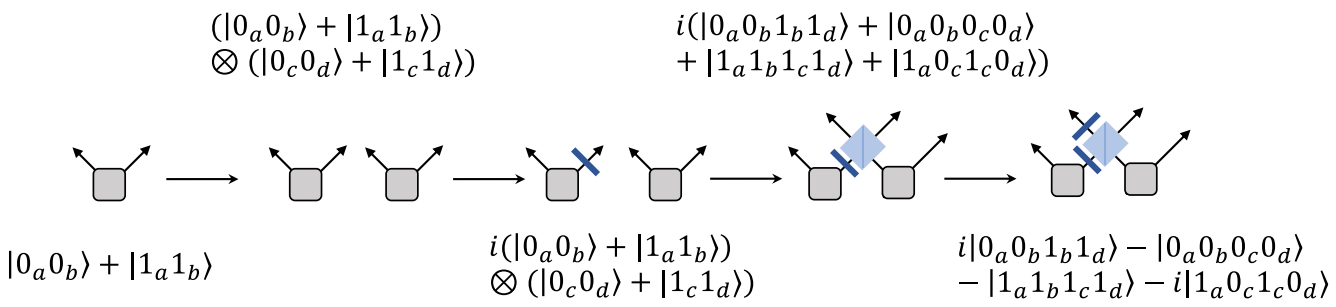

FIG. 1. Example of preparation of quantum state.

where θ represents the parameter of interest, such as a magnetic field, and H is the encoding Hamiltonian associated with it. Following this, the evolved state $\rho_\theta = S_\theta(\rho)$ is measured against an observable operator O, yielding a *response function* expressed as

$$R(\theta) = \mathrm{Tr}(O\rho_\theta). \tag{3}$$

To illustrate, given $H = \sum_{i=1}^{N} Z_i$ and $O = \otimes_{i=1}^{N} X_i$, as well as the probe state $\rho = |\psi\rangle\langle\psi|$ with $|\psi\rangle = (|0\rangle^{\otimes N} + e^{i\gamma}|1\rangle^{\otimes N})/\sqrt{2}$, the response function is $R(\theta)^2 = \cos N\theta$. The primary objective here is to estimate θ with the highest precision from $R(\theta)$, thereby minimizing the uncertainty $(\Delta\theta)^2$.

In an experiment, the measurement outcome x is influenced by the parameter θ, and the conditional probability distribution of x for a given θ is denoted as $p(x|\theta)$. The Fisher information [45] for the parameter θ is defined as

$$F(\theta) = \mathbb{E}\left[\left(\frac{\partial \log p(x|\theta)}{\partial\theta}\right)^2\right], \tag{4}$$

which quantifies the sensitivity of x to changes in θ. For an unbiased estimator $\tilde{\theta}$ of θ derived from measurement results $\{x_1, \ldots, x_M\}$ over M experiments, the Cramer-Rao bound (CRB) [46] holds:

$$(\Delta\theta)^2 \geqslant \frac{1}{MF(\theta)}. \tag{5}$$

In a quantum context, the sensitivity of x is inherently associated with the measurement process. For a parameterized quantum state ρ_θ, the Fisher information can be maximized over all possible POVMs E_x, leading to the quantum Fisher information (QFI) [47]:

$$F_Q(\rho_\theta) = \max_{\{E_x\}} F(\theta). \tag{6}$$

Subsequently, the quantum Cramer-Rao bound (QCRB) is

$$(\Delta\theta)^2 \geqslant \frac{1}{MF(\theta)} \geqslant \frac{1}{MF_Q(\rho_\theta)}. \tag{7}$$

Given a fixed probe state, this bound indicates the ultimate precision regardless of measurement.

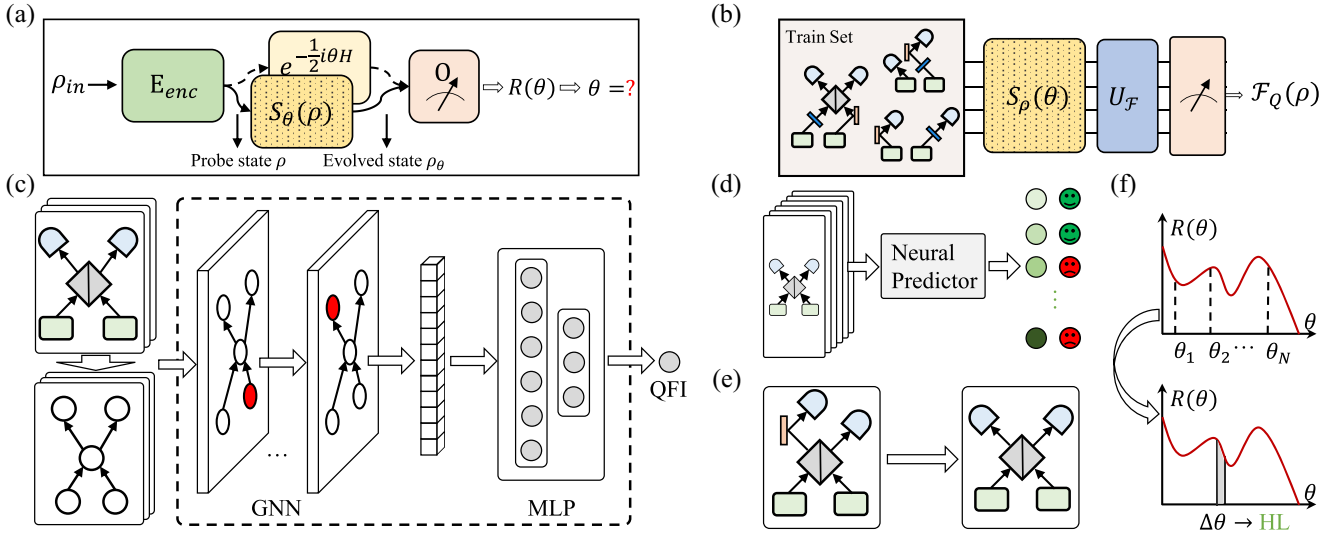

FIG. 2. Schematic of deep-learning-based quantum sensing. (a) Optical quantum sensing. The probe state ρ, prepared by an optical setup, is sent through a channel $S_\theta(\rho)$ that encodes parameter θ and then measurement operator O, resulting in a response function $R(\theta)$. We distinguish between channels under agnostic environments [an implicit form $S_\theta(\rho)$] and informed environments [an explicit form $S_\theta(\rho) = e^{-\frac{1}{2}i\theta H}\rho e^{\frac{1}{2}i\theta H}$] using a dotted yellow box for the former and a solid yellow box for the latter. (b) Data collection. Quantum Fisher information of a probe state is obtained via queries to an oracle $\mathcal{U}_{\mathcal{F}}$. (c) Training. A graph neural network (GNN) and a multilayer perceptron (MLP) are trained to predict the quantum Fisher information on labeled data. (d). Randomly sample massive unlabeled setups and use pretrained GNN to rank the QFI of them. (e) Fine tuning. Fine tune the selected setups, such as the layout and devices, and remove unnecessary ones. (f) Response inferring. Use trigonometric interpolation to infer the response function $R(\theta)$ and analyze the uncertainty $\Delta\theta$ of it.

By introducing the symmetric logarithmic derivative operator L_θ as

$$\frac{\partial \rho_\theta}{\partial \theta} = \frac{1}{2}(L_\theta \rho_\theta + \rho_\theta L_\theta), \tag{8}$$

it can be demonstrated that

$$F_Q(\rho_\theta) = \mathrm{Tr}\left(\rho_\theta L_\theta^2\right). \tag{9}$$

If the evolution of interaction is unitary, i.e., $\rho_\theta = e^{i\theta H}\rho e^{-i\theta H}$, F_Q does not depend on θ. Given the Hamiltonian H and the probe state $\rho = \sum_n b_n |\Phi\rangle\langle\Phi_n|$, the explicit form of F_Q is

$$F_Q = 2\sum_{i\neq j}\left(\frac{(b_i - b_j)^2}{b_i + b_j}|\langle\Phi_i|H|\Phi_j\rangle|\right). \tag{10}$$

For a pure state, namely, $\rho = |\Psi\rangle\langle\Psi|$, a simpler expression is

$$F_Q = 4(\Delta H)^2, \tag{11}$$

where $(\Delta H)^2 = \langle (H - \langle H\rangle)^2\rangle$.

For probe states with classical correlations, such as a tensor product of single-qubit states, the QFI scales linearly with the qubit number N, namely, the standard quantum limit (SQL). However, for optimal entangled probe states, the QFI scales quadratically with N, which is related to Heisenberg limit (HL) and gives the quantum advantage in sensing precision.

To sum up, the estimator of parameter needs to be optimal to saturate the CRB. And to make CRB reach the QCRB, the probe state also needs to be optimal. Therefore, to minimize parameter estimation uncertainty, a fundamental requirement is identifying an optimal optical setup for the probe state preparation.

To formalize the search for an optimal optical setup, let us define the toolbox of optical devices as a set $\mathcal{T}$, and the devices correspond to the elements in it. Consequently, an optical setup comprising L devices can be represented as $\mathrm{E}_{\mathrm{enc}} \in \mathcal{T}^L$. Hence, the search task converges to the following:

$$\max_{\mathrm{E}_{\mathrm{enc}}\in\mathcal{T}^L} \mathcal{F}_Q[\mathrm{E}_{\mathrm{enc}}(\rho_{\mathrm{in}})], \tag{12}$$

which is locating the $\mathrm{E}_{\mathrm{enc}}$ within $\mathcal{T}^L$ that maximizes the corresponding QFI $\mathcal{F}_Q(\rho)$. Here we do not pose any constraints on $\mathrm{E}_{\mathrm{enc}}$, the space encompassing all possible setups is $|\mathcal{T}|^L$ given a maximum length L. Note that $|\mathcal{T}|$ may also grow with the number of qubits N. While a larger L leads to a larger search space, thereby increasing the likelihood of containing the optimal setup, it also significantly raises the complexity of the searching process. Therefore, the choice of L should correspond to the size of the device set $\mathcal{T}$ and the number of qubits N involved in the task. In practice, L is often restricted by the physical limitations of implementing optical setups, as demonstrated in previous experimental studies [48–50].

C. Difference between agnostic and informed environment

In the informed environment, the formalism of encoding Hamiltonian H is known and the optimal probe state can be calculated exactly. Yet in many practical cases, as illustrated in Fig. 2(a), H is agnostic, and the channel $S_\theta(\rho)$ acts as a "black box." Therefore, one has to derive the optimal probe state from information gained from $S_\theta(\rho)$. Such information can be obtained by an oracle $U_{\mathcal{F}}$, which can be a quantum or classical algorithm to estimate the QFI or relevant quantities, as shown in Fig. 2(b).

In this work, we consider the QFI as the information obtained from interactions. Through interactions where the probe state evolves under the Hamiltonian, QFI can be approximated using a small perturbation δ to the probe state:

$$I_\delta(\theta;\rho_\theta) = 8\frac{1 - F(\rho_\theta, \rho_{\theta+\delta})}{\delta^2}. \tag{13}$$

Here, F represents the fidelity between the evolved state ρ_θ and the slightly perturbed state $\rho_{\theta+\delta}$, converging to QFI as $\delta \to 0$ [51,52]. This can also be approximated by a substitute of QFI [53] or variational quantum algorithms [54]. In large quantum system, it will be intrinsically hard due to the exponential dimension of quantum system. However, if considering smaller quantum systems suitable for real-world applications, the computational overload is affordable.

III. DEEP-LEARNING-BASED QUANTUM SENSING

In this section, we introduce the deep-learning-based quantum sensing scheme (DQS). We start by discussing the graph representation of optical setups and the role of graph neural networks (GNNs) in processing this representation. Subsequently, we outline the framework of DQS.

A. Graph encoding and graph neural network

Inspired by the unidirectional propagation of light, we represent an optical setup as a directed acyclic graph $G(V, E)$ with V being nodes (devices) and E edges (connections). The devices are represented by an array of node features $\mathbf{X} = (\mathbf{x}_1, \ldots, \mathbf{x}_l, \ldots, \mathbf{x}_L)^T \in \mathbb{R}^{L\times d}$, where each device is represented as a vector $\mathbf{x}_v \in \{0, 1\}^{d_1+d_2}$. Here, $d_1 = |\mathcal{T}|$ bits serve as a one-hot encoding for the device type, while the remaining $d_2 = N$ bits function as positional encoding. The connections are represented by an adjacency matrix $\mathbf{A} \in \{0, 1\}^{L\times L}$, where $\mathbf{A}_{ij} = 1$ only if the jth device is connected to the ith device.

We employ a graph neural network (GNN) to process the graph representation. Typically, GNNs follow an iterative neighborhood aggregation scheme to capture the information within the nodes' neighborhood. The propagation for a node $v \in V$, at the kth layer in GNN, is represented as

$$\begin{aligned}\mathbf{m}_v^{(k)} &= \mathrm{AGGREGATION}^{(k)}\left(\left\{\mathbf{h}_u^{(k-1)} : u \in \mathcal{N}(v)\right\}\right),\\ \mathbf{h}_v^{(k)} &= \mathrm{COMBINE}^{(k)}\left(\mathbf{h}_v^{(k-1)}, \mathbf{m}_v^{(k)}\right),\end{aligned} \tag{14}$$

where $\mathbf{h}_v^{(k)}$ is the hidden representation of node v at kth layer, $\mathcal{N}(v)$ is the set of nodes neighboring to v, and $\mathrm{AGGREGATION}^{(k)}$ and $\mathrm{COMBINE}^{(k)}$ are message passing functions of GNN layer. To extract the graph-level representation $\mathbf{z}$, all node representations are summarized through the READOUT function:

$$\mathbf{z} = \mathrm{READOUT}\left(\left\{\mathbf{h}_v^{(k)} : v \in V\right\}\right), \tag{15}$$

where common readout functions like max pooling are utilized. We refer such graph level representation as "latent representation," which has a dimensionality of 256 in our model. This 256-dimensional latent vector serves as a learned

representation of the input data, enabling a consistent representation of optical setups of different lengths. We enhance our GNN with a graph transformer architecture [55], leveraging attention mechanisms for improved performance.

Post-GNN processing, a single-layer MLP acts as the neural predictor for QFI. The predictions of the QFI are made based on the 256-dimensional latent vectors:

$$g(\mathbf{z}) = \mathbf{w}^{\intercal}\mathbf{z} + \mathbf{b}, \tag{16}$$

where both $\mathbf{w}$ and $\mathbf{b}$ are parameters of MLP. We denote the combination of GNN and predictor $\mathcal{G}(\mathbf{X}, \mathbf{A})$.

B. Framework of DQS

The DQS scheme aims to find the optimal optical setups that maximize the QFIs as well as estimate the correct parameter of interest. As shown in Figs. 2(c)–2(f), the scheme of DQS comprises four stages: training, ranking, fine tuning, and response inference. We delve into these stages in the following.

Training. Using data set $\{X_i, A_i, \mathcal{F}(X_i, A_i)\}_{i=1}^{D}$, where $\mathcal{F}(X_i, A_i)$ represents labels collected from interactions with the target environment, the model $\mathcal{G}$ is trained via supervised learning. The objective is to minimize prediction error $\mathcal{L}$, formulated as

$$\min_{\mathbf{W}\in\mathcal{W}} \mathcal{L}(\mathbf{W}) = \frac{1}{D}\sum_{i=1}^{D}[\mathcal{G}(X_i, A_i) - \mathcal{F}(X_i, A_i)]^2, \tag{17}$$

where $\mathbf{W}$ is the weight of neural network $\mathcal{G}$.

Ranking. Post-training, the fixed model $\mathcal{G}$ predicts QFIs for a set of offline explored, unlabeled setups. Exploration strategies may involve randomly sampling numerous setups or updating a fixed number of setups via an evolutionary algorithm (see Appendix F), as illustrated in Fig. 2(d). Setups exhibiting the highest QFI are selected as prime candidates $(\mathbf{X}^*, \mathbf{A}^*)$.

Fine tuning. The candidates identified during ranking undergo further validation and evaluation. Moreover, these setups are optimized, as shown in Fig. 2(e), by eliminating redundant devices or adjusting their positions where feasible. The most effective setup is then selected to prepare the final probe state. The QFI of the candidates can be verified using fidelity estimation [Eq. (13)] or other methods. If the QFI approaches N^2, the setup is considered near optimal for the QCRB, although it may not always be strictly N^2. The optimized probe state is subsequently utilized for determining the measurement operator O. Please refer to Appendix H for the optimization of O.

Response inference. When deploying the final probe state to interact with an unknown Hamiltonian, the response function $R(\theta)$ remains implicit. To address this, as shown in Fig. 2(f), we employ a trigonometric polynomial of degree n to infer the response function, expressed as

$$R(\theta) = \sum_{s=1}^{N}[a_s\cos(s\theta) + b_s\sin(s\theta)] + c. \tag{18}$$

Using the $2N+1$ predefined parameters $\{\theta_k\}_{k=1}^{2N+1}$, the coefficients can be approximated via trigonometric interpolation [56]. Thereafter, for a new θ and its associated measurement output $\bar{R}$, the inferred value of θ is determined as $\tilde{\theta} = \arg\min_\theta |\tilde{R}(\theta) - \bar{R}|$ where $\tilde{R}(\theta)$ is the inferred response. Notably, the uncertainty (or sensitivity) can be estimated by

$$(\Delta\theta)^2 = \frac{1 - \left(\sum_{s=1}^{n}[a_s\cos(s\theta) + b_s\sin(s\theta)] + c\right)^2}{\left|\sum_{s=1}^{n} s[-a_s\sin(s\theta) + b_s\cos(s\theta)]\right|^2}. \tag{19}$$

The DQS scheme can be very flexible. For an in-depth explanation, refer to Appendix B.

IV. NUMERICAL RESULTS

In this section, we present comprehensive experiments to evaluate the performance of DQS. We begin by a conceptual analysis of DQS, then assess the effectiveness of the GNN in processing optical setups. Following this, we evaluate DQS in a simulated eight-photon quantum sensing task. For additional numerical experiment results, please refer to the Appendixes C to J.

A. Experimental setup

The GNN architecture is implemented using the PyG library [57]. Training employed gradient descent optimization with the Adam optimizer [58], setting the learning rate to 10^{-4} and weight decay to 10^{-5}. Training spanned 200 epochs with a batch size of 64, executed on an RTX2080 GPU using the PYTORCH library [59].

Due to absence of existing data sets, we generated an optical data set using a "symbolic algebra" simulation method [15,60]. We reserved 5000 data as the validation set and 10 000 data as the test set. In order to mimic practical constraints [48–50] and ensure simulation efficiency, we empirically set the maximum number of devices to $L = 15$ (apart from the photon source). Since the Hamiltonian H is agnostic, L is fixed across all settings. Each optical setup's configuration includes 3 to 15 devices uniformly sampled in number, with types randomly assigned. Notably, for N-photon task, we defined $H = \sum_{i=1}^{N} Z_i$ as the Hamiltonian of the target environment, where Z_i represents the Pauli-Z operator on the ith qubit. It is important to clarify that while this Hamiltonian form is utilized to generate the data set, it is not known to the DQS scheme. In Appendixes C–E, we consider other environmental settings. For implementation details, please refer to Appendix B.

B. Conceptual comparison with conventional computer-aided methods

Before delving into our experimental analysis, we provide a conceptual comparison between DQS and conventional simulation methods [61]. Figures 3(a) and 3(b), as well as Table I, contrast optical quantum sensing under known and unknown environmental conditions from an algorithmic perspective. With known H [Fig. 3(a)], determining the optimal ρ is straightforward through classical simulations by solving Eq. (10), and the corresponding optical setup can be derived from the explicit form of ρ. Conversely when H is unknown [Fig. 3(b)], it becomes infeasible to directly compute ρ, challenging traditional approaches. We term this scenario as "agnostic" in our study. Although QFI can be estimated through physical measurements involving interactions with H,

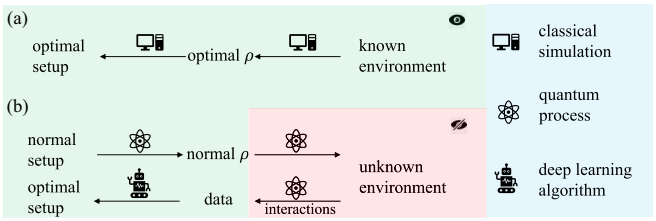

FIG. 3. (a) Conventional methods for known environments. (b) DQS for agnostic environments. Green areas represent the transparent aspects of optical quantum sensing, while red indicates the agnostic components.

this approach requires direct access to the physical system, which is not compatible with classical simulation.

The key feature of DQS is its environment-agnostic nature, meaning that it does not require explicit knowledge of H. Instead, the GNN in DQS is trained using data collected from past physical interactions with H. By leveraging the generalization capabilities of deep learning, the GNN can directly evaluate optical setups and estimate their effectiveness for QFI, effectively replacing traditional simulations without requiring explicit form of H. This makes DQS highly suitable for settings where the explicit form of H is inaccessible and where simulation-based methods are infeasible.

However, it is important to recognize that no single algorithm universally outperforms others across all scenarios. The No-Free Lunch theorem emphasizes that the effectiveness of an algorithm depends on the specific problem setting. For instance, in scenarios where the target environment can be effectively simulated or where utmost accuracy is crucial, simulation-based algorithms may be advantageous. Conversely, in contexts similar to ours where simulating the objective is impractical, deep-learning-based algorithms prove more suitable. This preference arises from deep learning's capability to extract insights from prior interactions with an agnostic environment, thereby optimizing the search for effective optical setups.

This nuanced comparison highlights the distinct advantages of our approach over simulation-based algorithms, particularly emphasizing the practical utility of deep-learning models in agnostic environments.

C. Performance of GNN predictor

To showcase the capabilities of our DQS algorithm, we begin by analyzing the behavior of the GNN in the latent space. We consider both four- and eight-photon tasks and the maximum setup length is 15. The GNN feature extractor transforms each setup into a 256-dimensional vector. Due to the complexities in visualizing high-dimensional data, we utilize the t-SNE method for dimensionality reduction, compressing the data into two dimensions [62]. It is important to note that the two-dimensional space is only for visualization, while the actual predictions are based on the full 256-dimensional latent space. In Figs. 4(a) and 4(c), data points of 10 000 test samples in the latent space are color coded according to their respective QFIs. The GNN successfully processes setups of various lengths and layouts, originally in disparate data formats, into uniform dimensional vectors, thereby facilitating subsequent analyses. Furthermore, the GNN cluster setups with higher QFIs within its latent space; for example, the right corner in the four-photon latent space and the left corner in the eight-photon space. From an information-processing perspective, the GNN retains relevant QFI details in its latent space while filtering out irrelevant data. Notably, the area with higher QFIs in the four-photon latent space is considerably larger than in the eight-photon space, reflecting the increasing difficulty of locating optimal probes as the number of qubits grows.

Next, we turn our attention to the MLP predictor. Figures 4(b) and 4(d) present the prediction results in the same latent spaces depicted in Figs. 4(a) and 4(c). The predicted QFIs closely align with the ground truth distribution. Importantly, even though the predicted QFI exhibits a small deviation, this does not impact the ranking phase, as the order of QFIs remains consistent within the highlighted regions of high-QFI setups.

Finally, we evaluate the GNN model's performance in relation to the size of the training data set. The aim is to identify the top-five candidate setups, according to the QFI, from a pool of 10 000 random test samples in each task. Figures 4(e)–2(g), corresponding to four-, six-, and eight-photon tasks, display the QFIs of the top-five setups as suggested by GNN models trained on varying data sizes, in comparison to the exact top-five setups in 10 000 test samples. The corresponding QFIs of the optimal probes in these tasks are 16, 36, 64, respectively. The results underscore the importance of data size. For instance, in the four-photon task, the model trained on only 1000 data points includes two setups with a QFI of zero among its top five, which is clearly not optimal. Similarly, in the six-photon task, the model trained on 1000 data points fails to identify the optimal setup, whereas the model trained on 5000 data points finds two, and the one trained on 10 000 finds four. As data size increases, so do the number of optimal setups among the top five candidates. We employ the Spearman correlation coefficient to illustrate the improvement in ranking quality as a function of increasing data size, as shown in the inset of Figs. 4(e)–2(g). To minimize the impact of training randomness, these coefficients are averaged from three independently trained GNNs. The required volume of data increases in proportion to the number

TABLE I. Required information for different algorithms. Check marks indicate components required by the algorithm, while cross marks indicate components that are not required.

	Optical setup	Form of ρ	Form of H	Interaction with H	Measurement O
Classical simulation	√	√	√	√	√
DQS	√	✗	✗	√	√

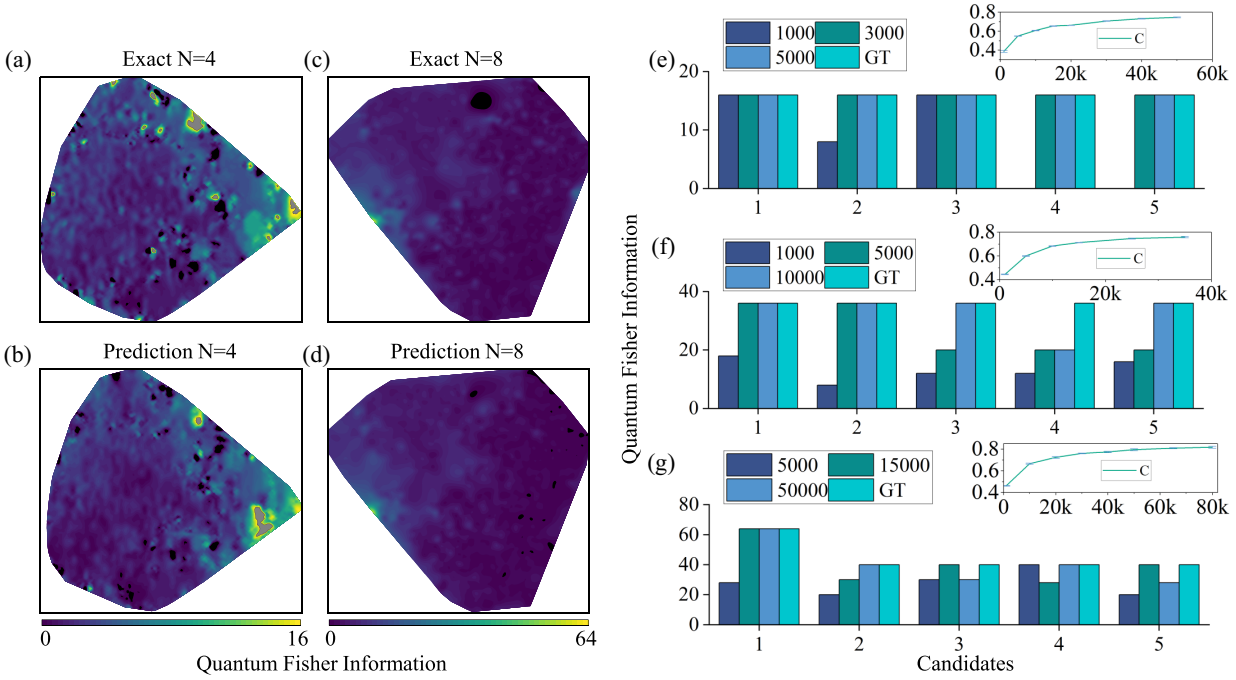

FIG. 4. Performance of DQS on different data sets. (a)–(d) Visualization of the latent space of GNN through t-SNE. (a), (c) Depict the latent spaces for four- and eight-photon setups, respectively. The color bar indicates the quantum Fisher information (QFI) levels. As evident in these figures, the graph neural network (GNN) maps each setup to a corresponding latent vector based on its QFI, clustering higher QFI values toward the corners of the latent space. (b), (d) Show GNN's QFI predictions in the respective latent spaces. (e)–(g) Performance analysis in relation to the size of the training data. The primary bar chart illustrates the top five setups selected from 10 000 random samples, based on models trained with varying data sizes, alongside the ground truth (GT) top five. (e)–(g) Correspond to tasks involving four, six, and eight photons. The inset graph elucidates the relationship between the Spearman correlation coefficients, "C" in the legend, and the sizes of the training data sets. The blue error bars indicate the standard deviation from three independently trained models.

of qubits, as the size of the search space expands. Accordingly, the GNN model requires more extensive data sets to ensure robust performance on unseen samples. To demonstrate the scalability of the DQS toward larger system, in Appendix F we show that adopting advanced exploration methods in the ranking step can effectively reduce the number of required training examples. Additionally, DQS's flexibility extends beyond the specific Hamiltonian used in this study, as demonstrated by its generalizability to other cases in Appendixes C–E.

D. Optimal eight-photon quantum sensing

We now turn our attention to an eight-photon quantum sensing task to investigate the overall performance for parameter estimation. In this context, we consider $H = \sum_{i=1}^{8} Z_i$ and $O = \otimes_{i=1}^{8} X_i$, which are not known to our model. In Appendix H, we introduce an empirical method to optimize O with respect to unknown H.

The GNN model under evaluation has been trained on 30 000 samples and is subsequently used to explore 50 000 new samples. We identify the top-three candidates, as illustrated in Figs. 5(a)–5(c):

(1) $\mathrm{PBS}_{b,c} \to \mathrm{PBS}_{a,g} \to \mathrm{QWP}_{h,0.5\pi} \to \mathrm{PBS}_{d,f} \to \mathrm{PBS}_{c,h} \to \mathrm{R}_d \to \mathrm{PBS}_{e,f} \to \mathrm{HWP}_{a,0.5\pi}$;

(2) $\mathrm{PBS}_{a,g} \to \mathrm{R}_c \to \mathrm{PBS}_{b,c} \to \mathrm{PBS}_{a,g} \to \mathrm{PBS}_{g,f} \to \mathrm{HWP}_{g,0.5\pi} \to \mathrm{HWP}_{d,0.5\pi} \to \mathrm{HWP}_{c,\pi} \to \mathrm{R}_b \to \mathrm{HWP}_{h,\pi} \to \mathrm{QWP}_{a,\pi}$;

(3) $\mathrm{PBS}_{f,d} \to \mathrm{R}_a \to \mathrm{PBS}_{a,e} \to \mathrm{QWP}_{b,0.25\pi} \to \mathrm{PBS}_{h,a}$.

The final state $|\psi\rangle$ and their corresponding QFI are as follows:

(1) $|\psi\rangle = [(1-i)|0\rangle^{\otimes 8} + (1+i)|1\rangle^{\otimes 8}]/2$ with QFI being 64;

(2) $|\psi\rangle = \frac{-1+i}{\sqrt{2}}(|0\rangle^{\otimes 4} + i|1\rangle^{\otimes 4})(|0\rangle^{\otimes 4} + |1\rangle^{\otimes 4})$ with QFI being 32;

(3) $|\psi\rangle = (i|0\rangle_b + |1\rangle_b)(|0\rangle^{\otimes 7} + |1\rangle^{\otimes 7})$ with QFI being 50.

The number of devices used in each setup is 8, 11, and 5, respectively. For comparative analysis, we also provide the best optical setup identified within the training data, depicted in Fig. 5(d), which serves as a result of the exhaustive search:

(1) $\mathrm{R}_b \to \mathrm{PBS}_{f,h} \to \mathrm{QWP}_{h,0.75\pi} \to \mathrm{QWP}_{f,\pi} \to \mathrm{PBS}_{d,h} \to \mathrm{QWP}_{e,0.5\pi} \to \mathrm{R}_c \to \mathrm{PBS}_{c,f} \to \mathrm{R}_f \to \mathrm{PBS}_{b,g} \to \mathrm{QWP}_{g,0.75\pi} \to \mathrm{R}_c \to \mathrm{HWP}_{h,5\pi}$.

The final state is $|\psi\rangle = (\frac{1-i}{\sqrt{2}}|0\rangle_g + \frac{i-1}{\sqrt{2}}|1\rangle_g)(|0\rangle^{\otimes 7} + |1\rangle^{\otimes 7})$ with QFI being 50. The number of devices is 13. In all setups, the subscripts denote specific device parameters and photon paths (from a to h). Additionally, the initial state prepared by SPDC forms a Bell state.

The first candidate is indeed an eight-qubit Greenberg-Horne-Zeilinger (GHZ) state, while others are tensor products of local GHZ states. The QFI of 64 indicates that our model finds the optimal optical setup in probe preparation. Notably, the probe state prepared by Fig. 5(d) exhibits a QFI of 50, meaning that none of the training samples possess

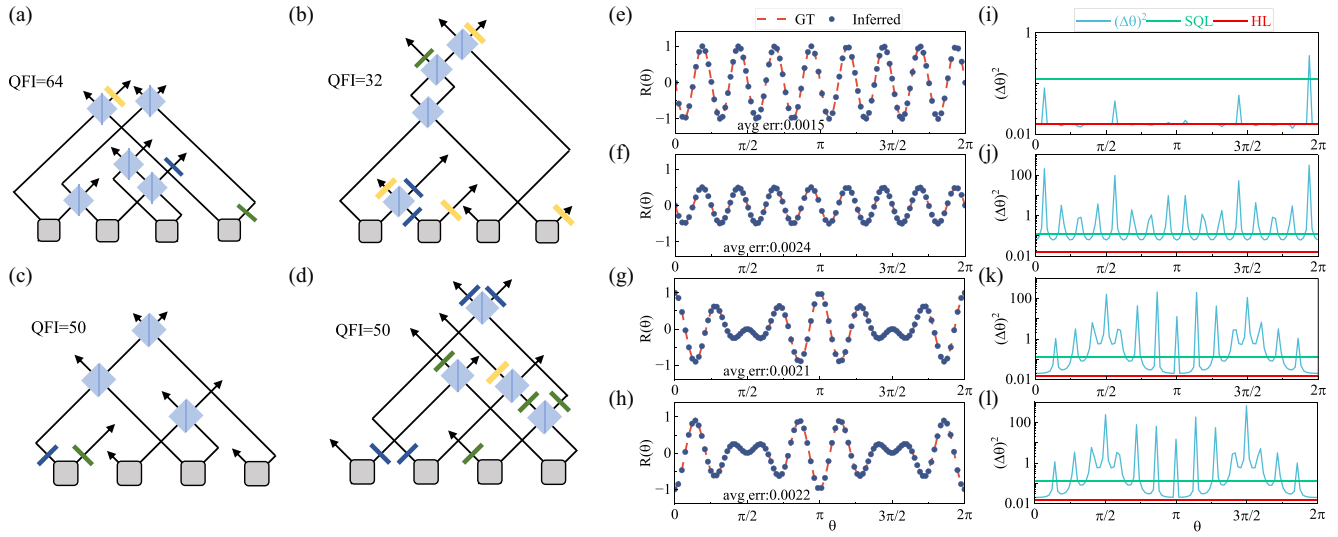

FIG. 5. Simulated results of an eight-photon quantum sensing task. (a)–(d) Experimental layout: present the layout of the top-three probe states identified during the testing phase by our method, while (d) shows the layout found within the training samples. The optical devices are represented as follows: DC (gray square), PBS (blue square), HWP (yellow rectangle), QWP (green rectangle), and R (deep blue rectangle). (e)–(h) Inferred response functions: display the inferred response functions corresponding to the layout shown in (a)–(d). The dashed red line represents the exact response function (GT), while the points indicate the inferred response. (i)–(l) Estimated sensitivity: exhibit the estimated sensitivities related to the layout depicted in (a)–(d). The blue curve indicates the sensitivity level, while the green and red lines mark the SQL and HL, respectively.

a QFI of 64 as Fig. 5(a). Despite the lack of exposure to the optimal setup during training, our model still manages to identify it among the unlabeled samples in the testing phase. This result highlights that the GNN model is in fact learning, rather than memorizing by rote, key structural patterns that contribute to QFI maximization, such as optimal utilization of beam splitters or wave plates, in an implicit way. In Appendix F, we demonstrate that using advanced methods rather than random sampling can reduce the number of explored samples by five times, thereby decreasing computational resources and enhancing the efficiency of DQS.

Subsequently, using these four prepared probes, the measurement output $\bar{R}(\theta)$ is collected, averaging over 10 000 shots results for each $\theta \in \{\theta_k\}_{k=1}^{2n+1}$ where $\theta_k = \frac{2\pi(k-1)}{2n+1}$. We employ the discussed trigonometric interpolation technique to approximate the response functions, as depicted in Figs. 5(e)–5(h). The optimal probe state prepared using our method yields response functions with minimal errors [Fig. 5(e), average error 0.0015], compared to the exhaustive search result [Fig. 5(h), average error 0.0022]. Interestingly, we observe error amplification at points with minimal derivatives, reflected by the concentration of points in small derivative intervals. This is consistent with the expectation that distinguishing between distinct θ values becomes challenging in regions of flat response.

Finally, we estimate the sensitivity of the whole quantum sensing scheme, as given in Eq. (19). We compare this estimated sensitivity against both the SQL (0.125) and the HL (0.016), as illustrated in Figs. 5(i)–5(l). Our proposed method closely approximates the HL across the majority of the interval, shown in Fig. 5(i), with minor deviations attributed to finite measurement shots. However, the best-performing setup from the training set, shown in Fig. 5(l), only approximates the HL within small intervals and frequently falls short of even the SQL. These results demonstrate that, with the same estimation method, the sensitivity of the quantum sensing scheme can still vary and even be inferior to classical sensors due to the suboptimal probe preparation. Regardless of the agnostic environment, our proposed DQS scheme manages to prepare the optimal probe and reach the HL in terms of sensitivity.

V. DISCUSSION

Our investigation illuminates the potential of deep learning in optical quantum sensing, especially in scenarios where a traditional scheme design falls short due to unknown target systems. The DQS scheme we have developed overcomes the challenge by offering an algorithmic scheme that not only learns to identify the optimal probes but also to estimate the target parameter to the Heisenberg limit (HL). The integrated GNN adeptly distills informative representations from the configurations of optical experiments, thereby amplifying the algorithm's efficacy in identifying optimal optical setups. Numerical experiments demonstrate the efficiency of our DQS method and its ability to evolve with increasing data. In a simulated eight-photon quantum sensing task, DQS achieves lower parameter estimation error compared to trivial quantum sensing scheme, and approaches HL in precision analysis. In a growing field where quantum technologies are becoming both more advanced and more complex, a scalable, data-driven approach for enhancing quantum sensing stands as a crucial advancement. As such, our work acts as a pivotal link between deep learning and quantum sensing, highlighting a

TABLE II. Toolbox of devices.

Device	Token	Visual	Operation	Operator
Spontaneous parametric down-conversion	DC($\|\psi\rangle, p, p'$)		$\|\psi\rangle \otimes \sum_l \|l\rangle_p \|l\rangle_{p'}$	$\mathrm{DC}_{p,p'}$
Beam splitter	BS($\|\psi\rangle, p, p'$)		$\|l\rangle_p \to \frac{\|l\rangle_p + i\|l\rangle_{p'}}{\sqrt{2}}$ $\|l\rangle_{p'} \to \frac{\|l\rangle_{p'} + i\|l\rangle_p}{\sqrt{2}}$	$\mathrm{BS}_{p,p'}$
Polarized beam splitter	PBS($\|\psi\rangle, p, p'$)		$\|l\rangle_p \to \|0\rangle_p$ when $l = 0$ $\|l\rangle_p \to \|1\rangle_{p'}$ when $l = 1$	$\mathrm{PBS}_{p,p'}$
Half-wave plate	HWP($\|\psi\rangle, p, \theta$)		$\|l\rangle_p \to O_{\mathrm{HWP}} \|l\rangle_p$ $O_{\mathrm{HWP}}(\theta) = \begin{bmatrix} \cos 2\theta & \sin 2\theta \\ \sin 2\theta & -\cos 2\theta \end{bmatrix}$	$\mathrm{HWP}_{p,\theta}$
Quarter-wave plate	QWP($\|\psi\rangle, p, \theta$)		$\|l\rangle_p \to O_{\mathrm{QWP}} \|l\rangle_p$ $O_{\mathrm{QWP}}(\theta) = \frac{1}{\sqrt{2}} \begin{bmatrix} 1 - i\cos 2\theta & -i \sin 2\theta \\ -i \sin 2\theta & 1 + i \cos 2\theta \end{bmatrix}$	$\mathrm{QWP}_{p,\theta}$
Mirror reflection	R($\|\psi\rangle, p$)		$\|l\rangle_p \to i\|l\rangle_p$	R_p

pathway for accelerated advancements in practical quantum technologies.

Despite the strides made with our DQS in enhancing the discovery of optimal quantum sensing schemes, certain limitations persist. First, our research scope did not encompass the design of the measurement operator. We exclusively utilized a basic Pauli operator, neglecting its pivotal role in achieving HL [1]. When delving into unknown environments, an intriguing avenue for future exploration is the development of adaptive measurement operators [63,64]. This would align the measurement with its probe and environment, potentially integrating into the DQS framework, thereby synchronizing the design for both probes and measurements. Second, accessing a quantum oracle to estimate the QFI remains a complex endeavor [51]. This is closely tied to accumulating training examples. Anticipated future research could explore efficient QFI data collection methodologies or even consider training deep-learning models with partial measurement results as label [65–68]. Lastly, our DQS strategy currently simply ranks random samples and picks the best candidates after the training phase. A potential enhancement could merge our model with extant optimization algorithms, such as evolutionary algorithms [15–18], further refining candidate searches. These future investigations will help build a more robust deep-learning-based quantum sensing scheme. In the Appendixes, we provide a brief case study for each discussed enhancement.

Beyond quantum sensing and optics, our research serves as a catalyst for novel explorations in harnessing deep-learning techniques to learn and predict quantum systems [30,36,40]. Two salient questions emerge: First, how can quantum-system-generated data be optimally represented for more effective learning? In DQS, we employ a graph format for depicting an optical setup, capturing both device data and layout dynamics. In contrast, outputs like shadow tomography [69,70] might better fit array representations and be used for certification task [71]. Second, how can deep-learning models be custom crafted for specific quantum systems? GNNs may be better suited for graph-structured data, like quantum circuits, over sequential data typified by measurement outputs. Moreover, the distinct characteristics of quantum-generated data necessitate strategic model training, warranting additional exploration.

ACKNOWLEDGMENTS

We thank X. Gu for helpful discussions on optical quantum experiments. This work was supported in part by NSFC Grant No. 62222117. X.-F.Y. acknowledges support from the China Postdoctoral Science Foundation (Grant No. 2023M733418). Dr. Tao's research is partially supported by NTU RSR and Start Up Grants.

APPENDIX A: OPTICAL DEVICES AND THEIR FUNCTIONALITY

In Table II, we define the optical devices in the toolbox in our quantum sensing setting.

APPENDIX B: IMPLEMENTATION DETAILS OF DQS SCHEME

The key feature of DQS is its flexible and modular algorithmic architecture. It incorporates a deep-learning model to discern patterns from data derived from environmental interactions, a search algorithm to explore potential optical setups, and an inference algorithm to implement the chosen setup and estimate θ. These components can be adapted based on a certain problem. In our work, DQS process leverages a graph neural network (GNN) to model geometric patterns of the optical setup and connect implicitly with the partial information obtained. It can seamlessly integrate with other advanced search algorithms, without further environmental interaction and conserving quantum resources. Once an optimal setup is identified, θ can be estimated using routine quantum sensing methods. In the following subsections, we introduce the building blocks in DQS.

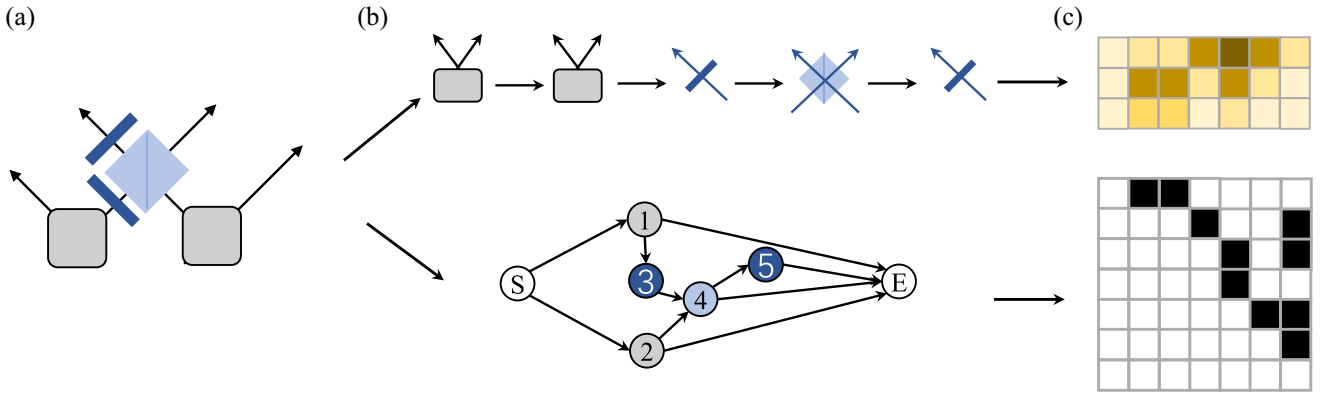

FIG. 6. Example of graph encoding of optical setup. (a) The layout of an optical setup. (b) The representation of sequence and directed acyclic graph, where the color of the node represents the type of optical device. (c) The sequence matrix $\mathbf{X}$ and and adjacency matrix $\mathbf{A}$. The color of the square represents the feature value accordingly.

1. Graph encoding of optical setup

We delve into the graph encoding of optical setups, as illustrated in Fig. 6. A setup can be characterized by the sequence of devices and their topological connections.

The sequence depicts the device order, which we represent as a matrix $\mathbf{X}$. This matrix is defined as $\mathbf{X} = (\mathbf{x}_1, \ldots, \mathbf{x}_l, \ldots, \mathbf{x}_L)^\intercal \in \mathbb{R}^{L\times d}$, as shown in Fig. 6(c). Each $\mathbf{x}_i$ within the matrix is a vector that represents the corresponding ith device in the sequence and is known as the feature vector. This vector is binary and consists of two components. The first part is a one-hot encoded vector (of length d_1) that identifies the device type. In this encoding, only one element is 1, while the others are 0. It is noteworthy that devices with varying parameters are distinguished. For instance, a QWP with $\theta = \frac{\pi}{4}$ and another with $\theta = \frac{\pi}{2}$ are considered different devices. In the main text, we consider a quantization of $\frac{\pi}{4}$ so there are four types of HWP and four types of QWP. Besides, we also treat DC with initial state $|00\rangle$, $|11\rangle$, and $|00\rangle + |11\rangle$ as three devices. Without any loss of generality, we also incorporate two unique devices: the start and end indicators. The second component is positional encoding. Here, each bit in the vector corresponds to a path. If a device interacts with path "a," then the associated bit in the vector (of length d_2) is set to 1; otherwise, it is set to 0.

The topological connection is defined using a directed acyclic graph (DAG) $G(V, E)$ with V denoting the node set and E the edge set. Every node corresponds to a device. An edge e_{ij} exists only if the jth device functions on the same path subsequent to the ith device. Every DC node is connected after the start node, and every node ends up with either the other device node or the end node. Here, we employ the adjacency matrix $\mathbf{A} \in \{0, 1\}^{L\times L}$ to represent G. In this matrix, $\mathbf{A}_{ij} = 1$ if and only if $e_{ij} \in E$.

2. Graph neural network

The graph neural network used in DQS scheme is structured into four components: embedding, graph transformer (message passing function), max pooling (READOUT function), and predictor as shown in Fig. 7. In the following, we detail the implementation of these four components. For clarification, all the $\mathbf{W}$ and $\mathbf{b}$ variables denote the adjustable weights of the neural network. Additionally, "Act" represents the activation function, and "BN" denotes the batch normalization function.

Embedding phase. This phase uses a single-layer MLP to transform the node feature vector, aligning it with the latent space. This transformation is given by

$$\mathbf{h}_i^{(0)} = \mathrm{MLP}_0(\mathbf{x}_i) = \mathrm{Act}[\mathrm{BN}(\mathbf{W}_0\mathbf{x}_i + \mathbf{b})], \tag{B1}$$

where the dimensions of $\mathbf{x}_i$ and $\mathbf{h}_i^{(0)}$ are d and s.

Graph transformer. Following the embedding phase, we employ alternating layers of graph transformers (GT) and MLPs to serve as the message passing mechanism. The lth is defined by

$$\mathbf{h}_i^{(l)} = \mathrm{MLP}_l\big[\mathrm{GT}_l\big(\mathbf{h}_i^{(l-1)}\big)\big]. \tag{B2}$$

Here, a C-head graph transformer is represented as

$$\hat{\mathbf{h}}_i^{(l)} = \mathrm{GT}\big(\mathbf{h}_i^{(l-1)}\big) = \mathrm{Concat}\big(\hat{\mathbf{h}}_i^{(l,1)}, \ldots, \hat{\mathbf{h}}_i^{(l,C)}\big). \tag{B3}$$

The output of the kth head can be defined by

$$\hat{\mathbf{h}}_i^{(l,k)} = \beta_i^{(l,k)}\mathbf{W}_1^{(l,k)}\mathbf{h}_i^{(l-1)} + \big(1 - \beta_i^{(l,k)}\big)\mathbf{m}_i^{(l-1,k)}, \tag{B4}$$

using aggregation

$$\mathbf{m}_i^{(l,k)} = \sum_{j\in\mathcal{N}(i)} \alpha_{i,j,k}^{(l)}\mathbf{W}_2^{(l,k)}\mathbf{h}_j^{(l-1)}, \tag{B5}$$

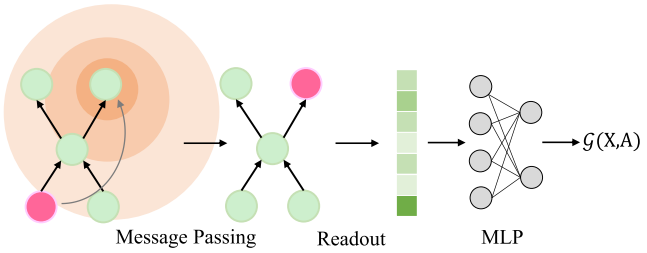

FIG. 7. Graph neural network. The information flows between node neighbors through the message passing stage. After the readout, the latent feature is sent to MLP to produce the final prediction $\mathcal{G}(\rho)$.

and attention coefficients

$$\alpha_{i,j,k}^{(l)} = \mathrm{softmax}\left(\frac{\left(\mathbf{W}_3^{(l,k)}\mathbf{h}_i^{(l-1)}\right)^{\intercal}\left(\mathbf{W}_4^{(l,k)}\mathbf{h}_j^{(l-1)}\right)}{\sqrt{s}}\right), \tag{B6}$$

alongside the skip information factor

$$\beta_i^{(l,k)} = \mathrm{sigmoid}\Big(\mathbf{w}_5^{(l,k)\intercal}\big[\mathbf{W}_1^{(l,k)}\mathbf{h}_i^{(l-1)}, \mathbf{m}_i^{(l,k)}, \mathbf{W}_1^{(l,k)}\mathbf{h}_i^{(l-1)} - \mathbf{m}_i^{(l,k)}\big]\Big). \tag{B7}$$

The MLP is defined by

$$\mathbf{h}_i^{(l)} = \mathrm{MLP}\big(\hat{\mathbf{h}}_i^{(l)}\big) = \mathbf{W}_7^{(l)}\big\{\mathrm{Act}\big[\mathrm{BN}\big(\mathbf{W}_6^{(l)}\hat{\mathbf{h}}_i^{(l)} + \mathbf{b}\big)\big]\big\} + \mathbf{b}. \tag{B8}$$

Max pooling. This phase merges all node vectors $(\mathbf{h}_1^{(N)}, \ldots, \mathbf{h}_L^{(N)})$ into a one-dimensional vector $\mathbf{h} \in \mathbb{R}^s$ by

$$\mathbf{h} = \mathrm{Max}\big(\mathbf{h}_1^{(N)}, \ldots, \mathbf{h}_L^{(N)}\big), \tag{B9}$$

where Max applies elementwise.

Predictor. Post-READOUT, a single-layer MLP acts as the neural predictor for QFI

$$\mathcal{G} = \mathbf{w}^{\intercal}\mathbf{h} + b. \tag{B10}$$

Here $\mathcal{G}$ is the prediction of QFI.

3. Training and data

Our model's architecture is based on five layers of graph convolution, each with a four-head transformer, with a latent dimension set to 256. The chosen activation function for the model is the GELU function [72] and the readout function used in the model is the max-pooling function.

The core objective of supervised learning is to train the neural network with labeled data sets in order to minimize prediction error. In this work, the loss function is given by

$$\mathcal{L}_{\mathrm{MSE}} = \mathbf{E}[\mathcal{G}(\mathbf{X}, \mathbf{A}) - \mathcal{F}(\mathbf{X}, \mathbf{A})]^2, \tag{B11}$$

where $\mathcal{F}(\mathbf{X})$ is the exact QFI.

Regarding the training process, we utilized the gradient descent optimization technique with the Adam optimizer [58]. We set the learning rate and weight decay at 10^{-4} and 10^{-5}, respectively. Our training consisted of 200 epochs with a batch size of 64. For the implementation of the model and the training process, we employed the PYTORCH library [59]. We have open sourced the code in Github Repo [73].

The data set for optical setups is created using a symbolic algebra-based tool [15]. This approach involves simulating the quantum operations of each optical device as defined in Table II. For instance, consider the sequence $\mathrm{DC}_{a,b} \to \mathrm{DC}_{c,d} \to \mathrm{PBS}_{b,c}$, which generates a four-qubit GHZ state. The first $\mathrm{DC}_{a,b}$ creates the Bell state $|0_a 0_b\rangle + |1_a 1_b\rangle$ across paths a and b, and the second $\mathrm{DC}_{c,d}$ creates the Bell state $|0_c 0_d\rangle + |1_c 1_d\rangle$ across paths c and d. The initial state is thus represented as a tensor product

$$(|0_a 0_b\rangle + |1_a 1_b\rangle) \otimes (|0_c 0_d\rangle + |1_c 1_d\rangle), \tag{B12}$$

which expands to

$$|0_a 0_b 0_c 0_d\rangle + |0_a 0_b 1_c 1_d\rangle + |1_a 1_b 0_c 0_d\rangle + |1_a 1_b 1_c 1_d\rangle. \tag{B13}$$

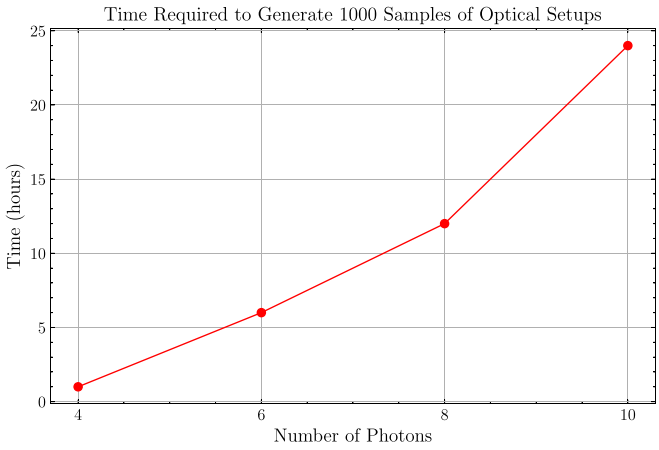

FIG. 8. Time for data generation with respect to photon size.

This symbolic polynomial representation, where each $|l\rangle_p$ is a variable for $l = 0, 1$ and $p \in a, b, c, d$, allows efficient simulation of operations like $\mathrm{PBS}_{b,c}$, which transforms terms based on specific rules (e.g., swapping $|l_b\rangle \leftrightarrow |l_c\rangle$ for $l = 1$). After this transformation, the resulting state becomes

$$|0_a 0_b 0_c 0_d\rangle + |0_a 0_b^2 1_d\rangle + |1_a 0_c^2 0_d\rangle + |1_a 1_b 1_c 1_d\rangle. \tag{B14}$$

Postprocessing, such as removing invalid terms due to Hong-Ou-Mandel (HOM) interference, results in the final GHZ state:

$$|0_a 0_b 0_c 0_d\rangle + |1_a 1_b 1_c 1_d\rangle. \tag{B15}$$

This symbolic algebra method enables efficient simulation of quantum setups by storing coefficients for each valid computational basis, which can then be used to calculate QFI for arbitrary Hamiltonians H using the stored state vector $|\psi\rangle$. The QFI is computed as

$$F_Q(|\psi\rangle, H) = 4[\langle\psi|H^2|\psi\rangle - (\langle\psi|H|\psi\rangle)^2]. \tag{B16}$$

This allows us to reuse the simulated optical setups for arbitrary Hamiltonian, enabling the collection of multiple QFI labels (e.g., for $H = \sum Z_i$, $H = \sum Y_i$, or $H = \sum X_i$). We implement this based on an open-source PYTHON implementation [60] and modify the definition of the optical devices according to Table II. We want to emphasize that future researchers aiming to replicate or build upon our work are not limited to this particular method. They can use any approach to produce data sets, provided that the resulting data aligns with the graph encoding structure we described. Figure 8 illustrates the runtime of the data-generation program relative to the photon number. This figure highlights the computational demands of generating large data sets for training the GNN as the system size increases. In real-world applications, real optical quantum computers could potentially accelerate data collection.

We would like to elucidate the difference between training samples, test samples, and explored samples:

(1) *Training samples*. Labeled data used to train the GNN via supervised learning, influencing its performance. The data set is generated using optical setups with a predefined length limit L. Consequently, the GNN is trained on a subset of

the possible configurations, rather than covering all possible setups.

(2) *Test samples*. Labeled data used solely to benchmark the GNN's performance. The number of test samples is fixed.

(3) *Explored samples*. Unlabeled setups explored during the ranking phase and used to find optimal setups under the guidance of the trained GNN. The ranking phase allows for more flexibility, including random sampling and advanced algorithms, enabling the exploration of setups with larger L than seen during training, which effectively expands the search space.

4. Ranking and fine tuning

In the ranking phase, we randomly sample a substantial amount of optical setups, denoted as $\{X_i, A_i\}_{i=1}^{D'}$. We use a trained GNN model to predict the QFI, represented as $\mathcal{G}(X_i, A_i)$. The results are ranked based on the predicted value, which is

$$i^* = \underset{i\in[D']}{\operatorname{argmax}}\, \mathcal{G}(X_i, A_i), \tag{B17}$$

where i^* represents the index of the optimal candidate.

Aside from random sampling, alternative methods can be utilized to reduce the computational resource. In Appendix F, we provide an evolutionary algorithm to facilitate the search of optimal candidates with GNN.

In the fine-tuning phase, given a candidate setup $X = (x_1, \ldots, x_L)^\intercal$, we randomly remove a device x_l (with $1 \leqslant l \leqslant L$). The setup X is then updated if the QFI remains unchanged. It is worth noting that, within the main content of the paper, we exhibit the original setups without any additional refinement in our results. However, this absence of modification bears no impact on the subsequent phase of response inference.

5. Response inferring

From the recent work by [56], response function $R(\theta)$ can be precisely expressed as a trigonometric polynomial function for $S_\theta(\rho) = e^{-\frac{1}{2}i\theta H}\rho e^{\frac{1}{2}i\theta H}$ such that $H = \sum_j h_j$ with $h_j^2 = I$ and $[h_j, h_{j'}] = 0,\ \forall\ j, j'$.

Theorem 1 (Theorem 1, [56]). The defined response function $R(\theta)$ can be exactly expressed as a trigonometric polynomial of degree n:

$$R(\theta) = \sum_{s=1}^{n}[a_s \cos(s\theta) + b_s \sin(s\theta)] + c, \tag{B18}$$

with $\{a_s, b_s\}_{s=1}^n$ and c being real-valued coefficients.

For trigonometric interpolation, the optimal approach is uniformly sampling the parameters as $\{\frac{2\pi(k-1)}{2n+1}\}_{k=1}^{2n+1}$.

The uncertainty or sensitivity of quantum sensing can be derived from error propagation $(\Delta\theta)^2 = [\Delta R(\theta)]^2/|\partial_\theta R(\theta)|^2$. This sensitivity is expressed in relation to the variance $[\Delta R(\theta)]^2 = \mathrm{Tr}[S_\theta(\rho)O^2] - \mathrm{Tr}[S_\theta(\rho)O]^2$ and the slope of $R(\theta)$. When $O^2 = I$, i.e., a Pauli string, this sensitivity can be represented as

$$(\Delta\theta)^2 = \frac{1 - \left(\sum_{s=1}^{n}[a_s \cos(s\theta) + b_s \sin(s\theta)] + c\right)^2}{\left|\sum_{s=1}^{n} s[-a_s \sin(s\theta) + b_s \cos(s\theta)]\right|^2}. \tag{B19}$$

Moreover, for approximation $\tilde{R}(\theta)$ and the corresponding sensitivity $\Delta\tilde{\theta}$, the estimation of sensitivity is related to the following theorem.

Theorem 2 (Theorem 4, [56]). Let $R(\theta)$ be the exact response function, and $\tilde{R}(\theta)$ be its approximation obtained from M-shot average $\overline{R}(\theta_k)$ with uniformly sample θ_k. Defining the maximum estimation error $\epsilon = \max_{\theta_k\in P}|R(\theta_k) - \overline{R}(\theta_k)|$, and the slope of $R(\theta$ at a field θ_k as $D_l = |\partial_\theta\tilde{R}(\theta)|_{\theta=\theta_l}|$, then

$$|\Delta\theta - \Delta\tilde{\theta}| \in O\left(\frac{\epsilon\log(n)}{D_l}\right). \tag{B20}$$

This indicates $\Delta\theta$ experiences fluctuations, especially in regions where the inferred response function's slope approaches zero.

APPENDIX C: PARAMETER QUANTIZATION

To transition a device with a continuous parameter into a one-hot vector representation, we discretize the possible angles of the wave plate within the range $[0, \pi]$. As delineated in the main text, we have confined the angle to the set $0°, 45°, 90°, 135°$. In this Appendix, we delve into a more fine-grained quantization of the device parameters. Specifically, we quantize the angle in increments of $2°$, encompassing potential angles of $0°, 2°, 4°, \ldots, 176°, 178°$.

For a comparative analysis, we employ the same four-photon task with $H = \sum_{i=1}^{4} Z_i$. The latent space induced by the GNN is illustrated in Fig. 9(a). It is evident that the transition from regions with lower QFI to those with higher QFI is more fluid in comparison to the results from the $45°$ configuration. This can be attributed to the refined quantization, which engenders a smoother QFI distribution within the latent space.

Figures 9(b) and 9(c) elucidate our model's performance relative to the size of the training data set. A salient observation here is that the model exhibits superior performance under the fine-grained parameter setting. The Spearman correlation coefficient between the predicted and true QFI is notably higher compared to the results from the $45°$ configuration. This might stem from the fact that a more diverse set of labels during training forces the model to master a robust predictor.

APPENDIX D: OTHER ENCODING HAMILTONIAN

The DQS does not depend on the explicit form of the encoding Hamiltonian, indicating its capability to discover the optimal probe state for various Hamiltonians. In this context, we consider a scenario where the parameter is encoded by the Hamiltonian $H = \sum_{i=1}^{4} X_i$.

Figures 10(a) and 10(b) showcase the performance of the GNN in terms of QFI prediction and the search of the optimal probe state and optical setup. The prediction of QFI exhibits deviation from the exact value. Also, the number of training examples required is considerably higher compared to the case with $H = \sum_{i=1}^{4} Z_i$. These findings suggest that the difficulty of seeking the optimal probe can differ based on the Hamiltonian.

Specifically, we consider 10 000 test examples with only one optimal optical setup with QFI being 16. The initial

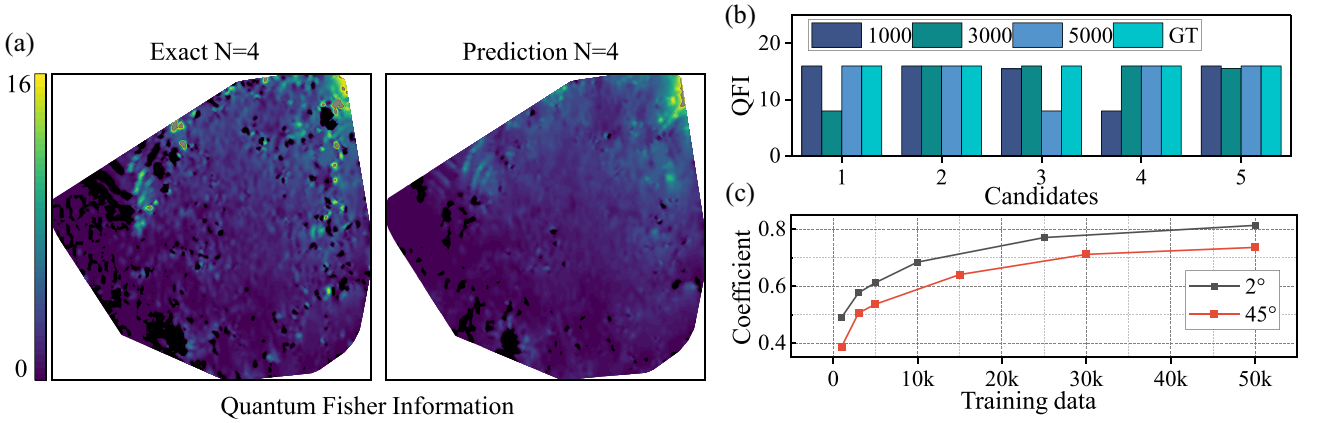

FIG. 9. (a) Latent space visualization. On the left, exact QFIs for four-photon optical setups are depicted, while on the right, the GNN predictions are shown. (b) Variation of top-five candidates with training data size. The bars reflect the QFIs of the top-five candidates from a pool of 10 000 test examples. These candidates are identified by a model trained on data sets of 1000, 3000, and 5000 examples, juxtaposed against the ground truth. (c) Spearman's correlation coefficient between predicted with ground truth QFIs. The black and red lines represent the correlation coefficients for the 2° and 45° quantizations, respectively, and how they evolve with the volume of training data.

10 000 training examples lack any setup with this QFI. Upon adding another 15 000 examples, which include two optimal setups, the trained model still fails to identify the optimal test setup. We then continue to add 25 000 training examples without optimal setups. This time, the trained model successfully discovers the optimal setup. These observations imply that the GNN is not simply memorizing the layouts of optimal setups but learning their pattern even from suboptimal examples.

In Fig. 11, we detail the corresponding layouts of the training's optimal setups and the test's optimal one. Device sequences for the different setups are as follows:

(a) $\mathrm{QWP}_{d,0.25\pi} \to \mathrm{PBS}_{b,c} \to \mathrm{PBS}_{d,a} \to \mathrm{R}_d \to \mathrm{HWP}_{c,\pi} \to \mathrm{BS}_{d,a} \to \mathrm{HWP}_{d,0.25\pi} \to \mathrm{BS}_{c,b} \to \mathrm{BS}_{b,d} \to \mathrm{R}_a \to \mathrm{HWP}_{b,0.25\pi} \to \mathrm{BS}_{d,b}$ with SPDC initial state $|\psi\rangle = (|0_a 0_b\rangle + |1_a 1_b\rangle)(|0_c 0_d\rangle + |1_c 1_d\rangle)$.

(b) $\mathrm{HWP}_{d,0.75\pi} \to \mathrm{R}_c \to \mathrm{HWP}_{d,0.5\pi} \to \mathrm{BS}_{c,d} \to \mathrm{R}_b \to \mathrm{BS}_{b,a} \to \mathrm{PBS}_{b,a} \to \mathrm{BS}_{b,d} \to \mathrm{BS}_{a,c} \to \mathrm{R}_a \to \mathrm{R}_d \to \mathrm{QWP}_{a,0.75\pi} \to \mathrm{R}_b$ with SPDC initial state $|\psi\rangle = (|0_a 0_b\rangle + |1_a 1_b\rangle)|1_c 1_d\rangle$.

(c) $\mathrm{R}_d \to \mathrm{BS}_{d,a} \to \mathrm{HWP}_{d,0.25\pi} \to \mathrm{R}_b \to \mathrm{BS}_{a,d}$ with SPDC initial state $|\psi\rangle = (|0_a 0_b\rangle + |1_a 1_b\rangle)(|0_c 0_d\rangle + |1_c 1_d\rangle)$.

The probe states are $|\psi\rangle = \frac{1}{\sqrt{2}}(|++++\rangle + e^{-i\gamma}|----\rangle)$ with different phases γ where $|+\rangle$ and $|-\rangle$ are the eigenvector of Pauli X. The discovered optical setup in the test phase is notably more simple than setups seen during training, aligning with our previous analysis of the GNN's behavior.

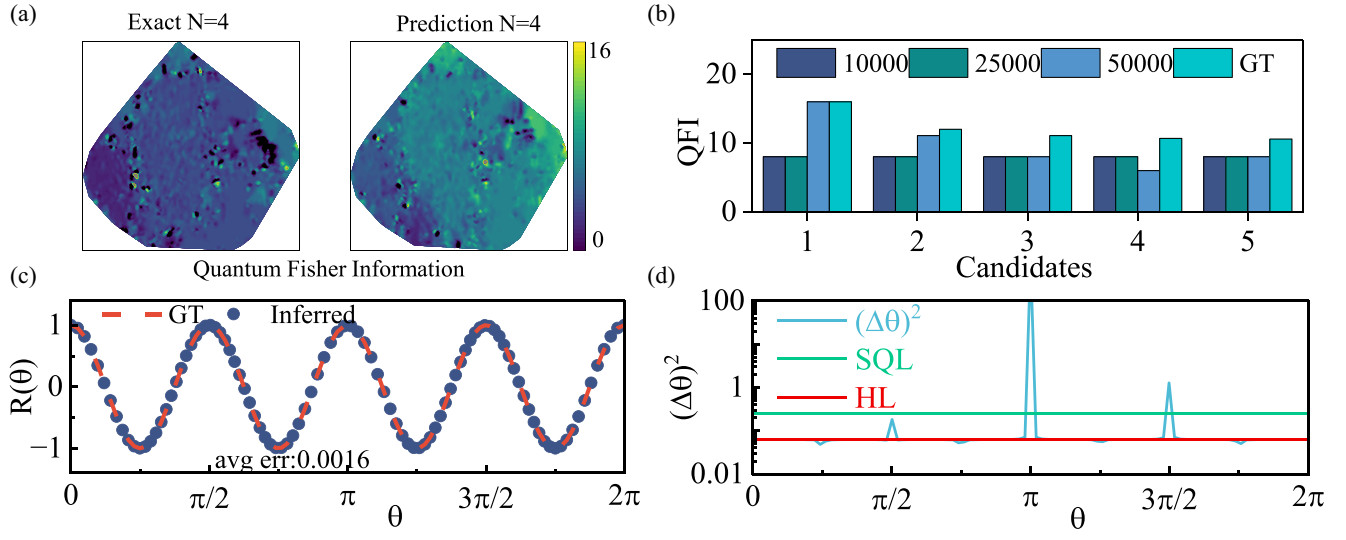

FIG. 10. (a) Latent space visualization. On the left, exact QFIs for four-photon optical setups are depicted, while on the right, the GNN predictions are shown. (b) Variation of top-five candidates with training data size. The bars reflect the QFIs of the top-five candidates from a pool of 10 000 test examples. These candidates are identified by a model trained on data sets of 10 000, 25 000, and 50 000 examples, juxtaposed against the ground truth. (c) Inferred response functions. The inferred response function corresponds to the layout shown in Fig. 11(c). The dashed red line represents the exact response function, while the points indicate the inferred response. (d) Estimated sensitivity. The blue curve indicates the sensitivity level, while the green and red lines mark the SQL and HL, respectively.

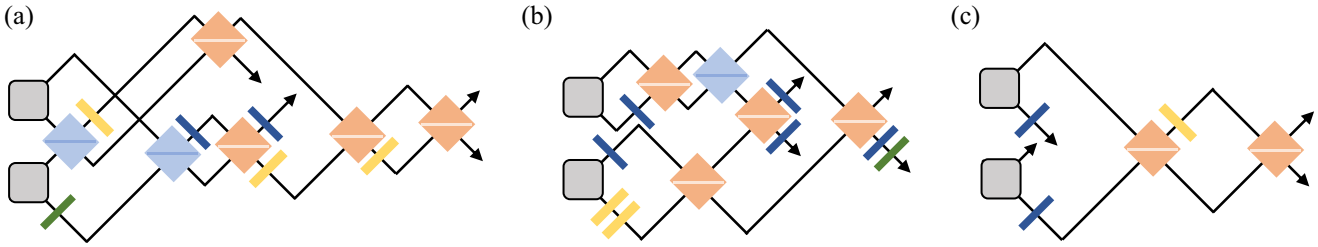

FIG. 11. (a), (b) Illustration of optimal examples during the training phase. (c) Identified optimal setups during testing.

For the quantum sensing task, we employ the measurement operator $O = \otimes_{i=1}^{4} Z_i$ for the quantum sensing task. In Figs. 10(c) and 10(d), we depict the inferred response function and the estimated sensitivity. The mean error is 0.0016, while the sensitivity achieves the Heisenberg limit.

APPENDIX E: TWO-PHOTON INTERACTION

In this Appendix, we delve into the encoding Hamiltonian that encompasses two-photon interactions, specifically represented as $H = \sum_{i<j} X_i X_j$. As depicted in Fig. 12, the GNN demonstrates proficiency in retrieving optimal setups even with a modest volume of training data. However, it is noteworthy that the Spearman correlation coefficient for this is a little lower in comparison to the scenario involving a one-photon interaction.

While certain instances have been reported where precision surpasses the Heisenberg limit [74–76], they do not directly align with the context of our discourse. Our study is specifically bounded to situations that consider a singular measurement operator.

APPENDIX F: EVOLUTIONARY ALGORITHM IN EXPLORATION PHASE

The process of the evolutionary algorithm for identifying optimal optical setups is summarized as follows [77]:

(1) *Initialization*. Initiates with the generation of a "population" of candidate optical setups randomly. This population is denoted as $D_0 = \{X_i\}_{i=1}^{N}$, where each $X_i = (x_1^{(i)}, \ldots, x_L^{(i)})$ constitutes the sequence of L optical devices for the ith setup, with each $x_j^{(i)}$ belonging to a set of device types $\mathcal{T}$. This foundational step populates the evolutionary process with a diverse array of starting configurations.

(2) *Fitness evaluation*. In each time step t in iteration, assigns a "fitness" score $f(X_i)$ to each setup X_i in current population D_t, indicative of its efficacy, which in our experiments is quantified by the quantum Fisher information (QFI). This evaluation is performed either by querying the oracle $U_{\mathcal{F}}$ or employing the trained GNN model $\mathcal{G}$. A higher fitness score enhances the probability of selection for reproduction.

(3) *Selection*. Based on fitness scores, candidates are selected for breeding, with a preference for those exhibiting higher fitness. This process involves tournament selection, where for each of the total $|D_t|$ tournaments, a subset of k optical setups is randomly chosen, and the setup with the highest fitness score is selected for the next generation. The parameter k typically ranges from 1 to 3.

(4) *Crossover*. In this step, selected setups are paired, and segments of their sequences are exchanged to create offspring with a probability p_c. Specifically, for paired sequences X_i and X_j of lengths L_i and L_j, respectively, and assuming $L_i < L_j$, two integers $1 < m < n < L_1$ are chosen randomly. The segments from the mth to nth devices are swapped between X_i and X_j, resulting in new sequence combinations. This crossover introduces unique device arrangements into the population, fostering the exploration of uncharted configurations.

(5) *Mutation*. Offspring may undergo mutations with a probability p_m, involving random alterations to the devices within the setups, such as changes, additions, or deletions of devices. Each device-wise alternation has an individual probability p_d. This mutation process is applied to all offspring, ensuring genetic diversity and averting premature convergence on suboptimal solutions.

(6) *Replacement*. The newly created individuals from the crossover and mutation phases form the next generation, G_{t+1}, updating the population for the ensuing evolutionary cycle and progressively refining the search for optimal setups.

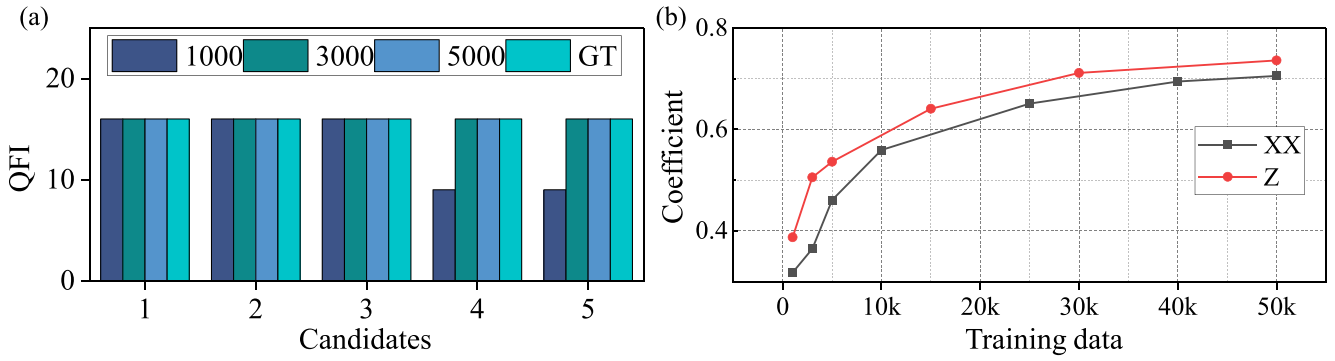

FIG. 12. (a) Performance with respect to training data size. (b) The Spearman coefficient between predicted QFIs and ground truth on 10 000 test examples.

TABLE III. Numerical results of using evolutionary algorithm as sampling method. Here, D refers to the population size, T refers to the time steps, and k refers to the tournament selection factor. "Y" indicates that there are optimal setups in the final population, otherwise it is "N." QFI is the quantum Fisher information of the optimal setup in them.

No.	Data set size	D	T	k	Is optimal	QFI
1	30 000	1000	50	1	Y	64
2	30 000	100	500	1	N	24
3	30 000	1000	100	1	Y	64
4	30 000	200	50	1	N	40
5	30 000	1000	50	2	Y	64
6	30 000	100	500	2	Y	64
7	30 000	500	50	2	Y	64
8	30 000	200	50	2	Y	64
9	30 000	200	50	3	Y	64
10	10 000	1000	50	2	Y	64
11	10 000	200	50	2	Y	64
12	5000	1000	50	2	Y	64
13	5000	200	50	2	N	34

(7) *Termination*. The evolutionary cycle of evaluation, selection, crossover, mutation, and replacement continues until a predetermined stopping condition, such as a fixed number of iterations T, is reached.

The parameters of evolutionary algorithm include the population size $|D_t|$ at each step, the number of evolving steps T, the tournament selection factor k, and the crossover and mutation probability p_c, p_m, and p_d. These parameters will eventually decide the performance of the algorithm. Specifically, assuming $|D_t| = D$ $(0 \leqslant t \leqslant T)$, the algorithm involves totally $D \times T$ fitness evaluation, which roughly decides the runtime of it.

Now we numerically compare the evolutionary algorithm (EA) and random sampling for exploration with the trained GNN. The implementation of evolutionary algorithm is based on DEAP PYTHON library [78]. Key parameters for the evolutionary algorithm include a crossover probability of $p_c = 0.5$, a mutation probability of $p_m = 0.2$, and an individual probability of $p_d = 0.05$. We adjust the population size $|D|$ and the step size T to modulate the overall number of evaluations.

In this analysis, we revisit the configuration of $H = \sum_{i=1}^{8} Z_i$ outlined in the main text. Previously, the GNN, trained on 30 000 samples, was adept at identifying an optimal setup within 50 000 new samples without having encountered any optimal configurations during its training phase. For a balanced comparison, we employ the identical GNN model trained on the same data set of 30 000 samples. The outcomes of utilizing the EA to navigate the solution space are summarized in Table III. To modulate the total number of explored optical setups $(D \times T)$, we adjust the population size D and the time step T. In the initial two experiments, we configure $D = 1000, T = 50$ and $D = 100, T = 500$, ensuring the total number of setups matches the 50 000 figure from random sampling. Moreover, the tournament selection factor is set to 1 to minimize selection pressure and foster diversity. In the first experiment, the optimal setup is pinpointed. However, in the second experiment, the highest QFI observed is only 24. These two configurations of D and T emphasize the balance between exploration and exploitation: a larger population size (D) encourages broader exploration of the search space, whereas a higher number of evolution steps (T) gears towards intensive exploitation within the current population. In Fig. 13, the top-three candidates identified by the EA under explorative [Figs. 13(a)–13(c) and exploitative Figs. 13(e) and 13(f)] settings are showcased. The sequences and their corresponding probe states are detailed as follows:

(a) $\mathrm{HWP}_{e,\pi} \rightarrow \mathrm{PBS}_{b,c} \rightarrow \mathrm{R}_h \rightarrow \mathrm{HWP}_{c,\pi} \rightarrow \mathrm{R}_h \rightarrow \mathrm{PBS}_{a,e} \rightarrow \mathrm{R}_a \rightarrow \mathrm{PBS}_{f,h}$ with probe state $|\psi\rangle = (|0\rangle^{\otimes 8} + |1\rangle^{\otimes 8})/\sqrt{2}$ and QFI being 64.

(b) $\mathrm{PBS}_{a,e} \rightarrow \mathrm{R}_e \rightarrow \mathrm{R}_f \rightarrow \mathrm{QWP}_{b,0.5\pi} \rightarrow \mathrm{R}_h \rightarrow \mathrm{QWP}_{b,0.5\pi} \rightarrow \mathrm{PBS}_{c,g} \rightarrow \mathrm{PBS}_{b,f} \rightarrow \mathrm{PBS}_{a,g}$ with probe state $|\psi\rangle = (|0\rangle^{\otimes 7} + |1\rangle^{\otimes 7})(|1_h\rangle + |0_h\rangle)/2$ and QFI being 50.

(c) $\mathrm{HWP}_{e,\pi} \rightarrow \mathrm{PBS}_{a,e} \rightarrow \mathrm{R}_a \rightarrow \mathrm{PBS}_{c,h} \rightarrow \mathrm{R}_h \rightarrow \mathrm{HWP}_{f,0.5\pi} \rightarrow \mathrm{PBS}_{g,h} \rightarrow \mathrm{R}_a \rightarrow \mathrm{PBS}_{b,f}$ with probe state $|\psi\rangle = (|0\rangle^{\otimes 4} + |1\rangle^{\otimes 4})(|0\rangle^{\otimes 4} + |1\rangle^{\otimes 4})/2$ and QFI being 32.

(d) $\mathrm{PBS}_{a,d} \rightarrow \mathrm{R}_d \rightarrow \mathrm{R}_f$ with probe state $|\psi\rangle = (|0\rangle^{\otimes 4} + |1\rangle^{\otimes 4})(|0\rangle^{\otimes 2} + |1\rangle^{\otimes 2})(|0\rangle^{\otimes 2} + |1\rangle^{\otimes 2})/2\sqrt{2}$ and QFI being 24.

(e) $\mathrm{R}_b \rightarrow \mathrm{R}_c \rightarrow \mathrm{R}_f$ with probe state $|\psi\rangle = |+\rangle^{\otimes 8}$ and QFI being 16.

(f) $\mathrm{R}_b \rightarrow \mathrm{R}_d \rightarrow \mathrm{R}_f$ with probe state $|\psi\rangle = |+\rangle^{\otimes 8}$ and QFI being 16.

The initial states prepared by spontaneous down-conversion (SPDC) are Bell states.

The results indicate a preference for exploratory settings by the algorithm, with exploitative settings likely leading to convergence on local optima. In a third experiment, by increasing the step size to 100 from the first experiment's setup, the EA still identifies optimal setups, having already found them within 50 steps. However, reducing the population size to 200 does not yield the discovery of the optimal setup, suggesting that with a weaker selection pressure, the EA requires more than 10 000 evaluations to locate the optimal configurations, which is close to random sampling.

To reduce the number of evaluations required, we enhance the tournament selection factor k to 2. In experiments 4 through 8, we adopt various configurations: $D = 1000, T = 50$; $D = 100, T = 500$; $D = 500, T = 50$; and $D = 200, T = 50$. Across all these settings, the EA successfully identifies the optimal setups within the specified

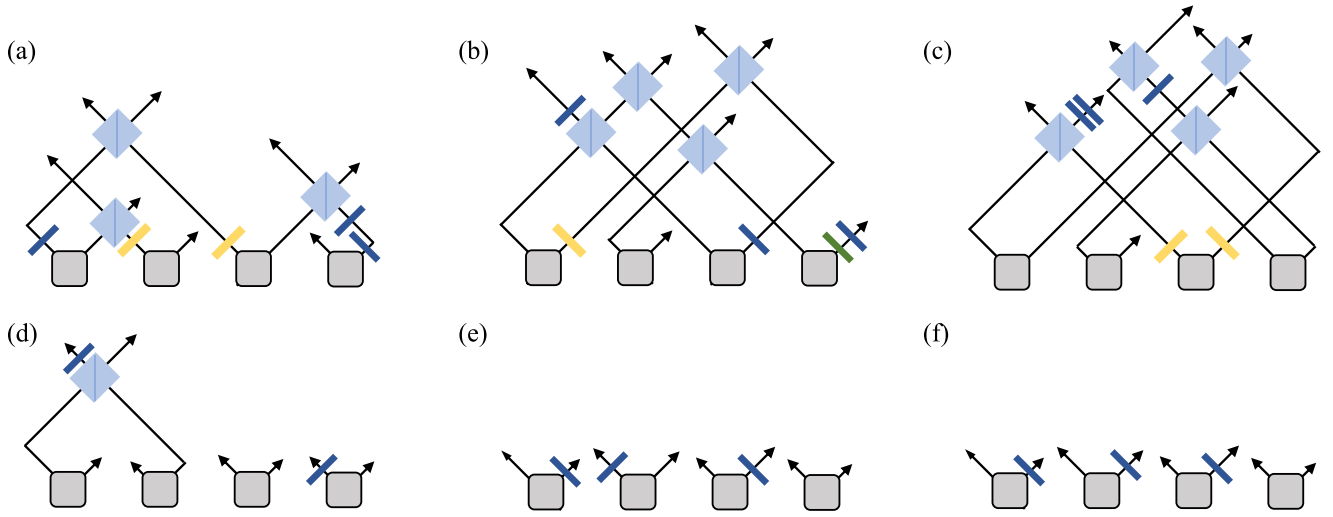

FIG. 13. (a)–(c) Illustration of top-three setups based on exploration. (d)–(f) Illustration of top-three setups based on exploitation.

evaluation limits. Proceeding to experiment 9, we escalate k further to 3, coupled with settings of $D = 200$ and $T = 50$. Remarkably, the EA continue to find optimal setups. The heightened selection pressure evidently compels the population to retain optical setups with higher QFI values while discarding those with lower performance at each evolutionary step.

While increasing k to 2 or 3 indeed streamlines the process of identifying a singular optimal setup, it is crucial to acknowledge the potential reduction in population diversity this strategy incurs. Notably, in the concluding stage of experiment 9, a significant portion of the optimal setups within the 200 setups are identical. In the realm of optical quantum sensing, the primary goal might often be to discover just one optimal configuration. Nonetheless, this approach presents a clear tradeoff for those aiming to unveil a broader spectrum of satisfactory setups.

The outcomes from experiments 8 and 9 illuminate that a mere 10 000 evaluations can suffice to identify optimal setups with the EA, provided the algorithm's parameters are properly selected. Notably, this number falls below the 30 000 labeled data instances used in the training phase. This revelation prompts an inquiry into the necessity of such a voluminous data set when employing EA post-training. To explore this, experiments 10 to 13 have been conducted using GNN models trained on data sets comprising 10 000 and 5000 samples, respectively. The GNN model conditioned on 10 000 samples successfully pinpointed the optimal setups within the evaluation bounds. Conversely, the model trained on a mere 5000 samples faltered in identifying the optimal configuration at $D = 200$, attributing to its weaker robustness with scarce training data. However, it achieved success upon expanding the evaluation limits, an endeavor that proves cost effective given the GNN's rapid execution speed. Each EA experiment leveraging the GNN unfolded within briefly 2 min, suggesting that enlarging D and T parameters could effectively safeguard performance metrics.

These findings also suggest that even though a GNN trained on a leaner data set might exhibit reduced accuracy, the relative order of predicted QFI scores is likely retained, enabling the EA to discern optimal setups efficiently. Furthermore, it is worth noting, as previously mentioned, the training data sets remain consistent with those described in the main text, wherein the GNN is not exposed to any optimal setups during its learning phase. This consistency underscores the GNN's aptitude for learning and generalization, rather than mere memorization of optical setup structures, showcasing its potent capability to identify optimal configurations absent prior exposure.

To encapsulate, incorporating an alternative methodology like the evolutionary algorithm for sampling can enhance the efficiency of the DQS framework. This enhancement is observed in the reduction of both the requisite size of training data and the scope of sampling. Given that the labeled training data necessitate collection via the oracle $U_{\mathcal{F}}$, employing such a strategy can markedly diminish interactions with the quantum environment, thereby conserving quantum resources. Additionally, this outcome underscores the inherently flexible and modular architecture of the DQS scheme, which accommodates the incorporation of sophisticated subroutines, further amplifying its utility and effectiveness in quantum sensing applications.

APPENDIX G: 10-PHOTON QUANTUM SENSING TASK

In this Appendix, we further study the performance of DQS on larger system.

We first assess the GNN predictor's performance in relation to the data set's scale used for training on 10-photon data set. The target Hamiltonian is still $H = \sum_{i=1}^{10} Z_i$. The GNN models are trained across data sets comprising 20 000, 40 000, and 80 000 samples. In all of the data sets there exists no optimal setup with QFI being 100. To ensure robustness and reliability of the results, each model undergoes a training process independently three times. After training, the models are evaluated against a collection of 10 000 random samples. It is noteworthy in this test set there is absence of any optimal setups, with the highest QFI being 68. This experiment aims to benchmark the GNN predictor's performance, where the lack

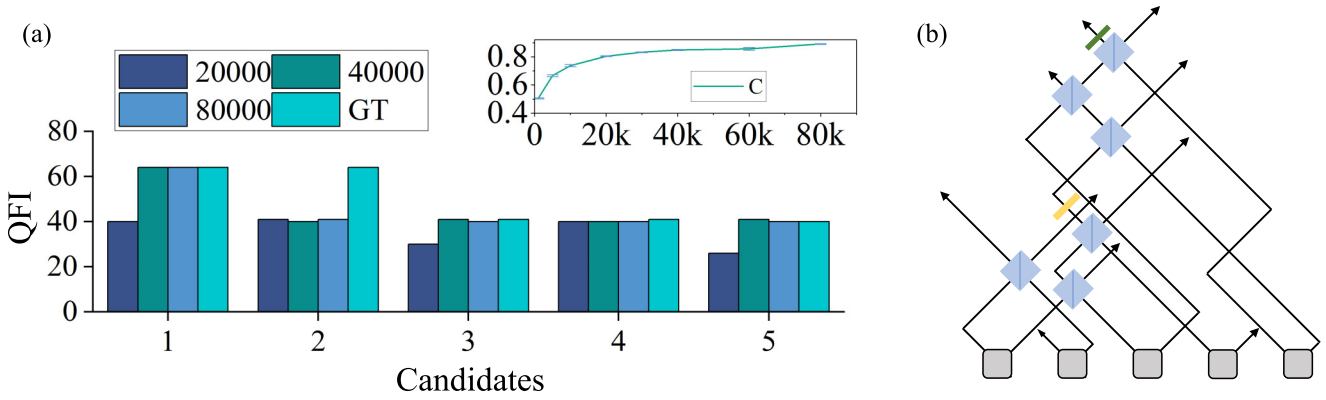

FIG. 14. (a) The primary bar chart illustrates the top-five setups selected from 10 000 random samples, based on models trained with varying data sizes 20 000, 40 000, 80 000, alongside the ground truth (GT) top five. The inset graph elucidates the relationship between the Spearman correlation coefficients (green line) and the sizes of the training data sets, where the error bars (in blue, but very small) indicate the standard deviation from three independently trained models. (b) Illustration of optimal setup identified with model trained on 20 000 examples.

of an optimal optical configuration in the test samples barely affects making conclusion from the outcomes.

Figure 14(a) displays the corresponding QFI of the top-five configurations selected from the 10 000 test examples by each of the models, in comparison with the precise top-five candidates. The models that underwent training with data sets of 40 000 and 80 000 samples successfully identified a setup featuring the largest QFI in the test ensemble, albeit not exhaustively, given the existence of two such configurations. This observation underscores the escalating complexity in precisely forecasting the QFI as the photon count increases. Embedded within Fig. 14(a), an inset graph plots the relation between the training data sets' sizes and the average Spearman correlation coefficients averagely evaluated from three independently trained GNN models. In alignment with findings articulated in the main text, this coefficient exhibits growth proportional to the increase in the training data-set size. Remarkably, although the GNN model trained with 20 000 samples fails to find the optical setup with highest QFI, it still demonstrated a Spearman coefficient nearly akin to that of the model trained with 80 000 samples, both above 0.8. This suggests that the prediction order of the former closely mirrors the truth values' order as effectively as the latter, highlighting the GNN's predictive power even with reduced training data size.

We then adopt the GNN model trained on 20 000 samples and combine it with the EA introduced previously to search for the optimal setup. Here we set population size $D = 1000$, step size $T = 50$, and tournament selection factor $k = 2$. In Fig. 14(b), we report the best optical setup in the final population. The corresponding device sequence is $\mathrm{PBS}_{b,e} \to \mathrm{PBS}_{a,d} \to \mathrm{PBS}_{e,g} \to \mathrm{HWP}_{g,\pi} \to \mathrm{PBS}_{g,n} \to \mathrm{PBS}_{f,n} \to \mathrm{PBS}_{f,m} \to \mathrm{QWP}_{m,\pi}$ with probe state $|\psi\rangle = (|0\rangle^{\otimes 10} + |1\rangle^{\otimes 10})/\sqrt{2}$ and QFI being 100. The corresponding QFI means the optical setup we find is indeed optimal, which highlights the efficacy of our algorithm enhanced by the EA.

Following the setting of the main text, we employ the found optical setup to perform the quantum sensing task. We first consider the observable $O = \otimes_{i=1}^{10} X_i$. In Fig. 15, we report the inferred response function using the trigonometric interpolation method and the estimated sensitivity. As shown in Fig. 15(a), the response function has a small average error of 0.0018. In Fig. 15(b), the displayed sensitivity curve is aligned with the Heisenberg limit (0.01), with only negligible fluctuation at the point with small derivative.

APPENDIX H: OPTIMIZATION OF OBSERVABLE OPERATOR

In the previous Appendix, the given O is already optimized with respect to the probe state and the Hamiltonian. Since we aim at agnostic environment, here we present an empirical method to optimize the O. Consider a parametrized local observable $U(\mathbf{x}) = aX + bY + cZ$, a linear combination of Pauli matrices, where X, Y, and Z are Pauli matrices and $\mathbf{x}$

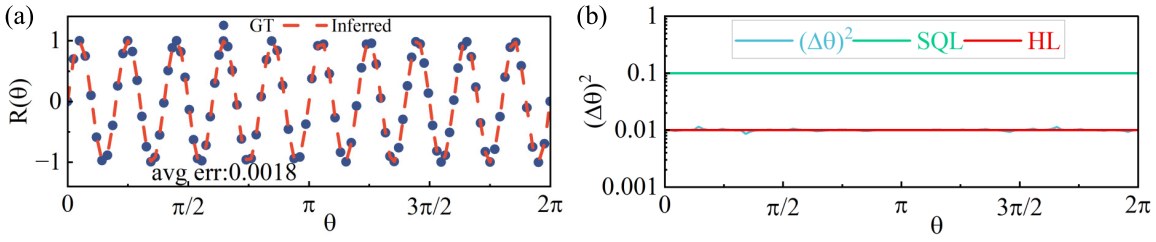

FIG. 15. (a) Inferred response functions corresponding to the layout shown in Fig. 14(b) with observable being $O = \otimes_{i=1}^{10} X_i$. The dashed red line represents the exact response function (GT), while the points indicate the inferred response. (b) The estimated sensitivities related to the response function. The blue curve indicates the sensitivity level, while the green and red lines mark the SQL and HL, respectively.

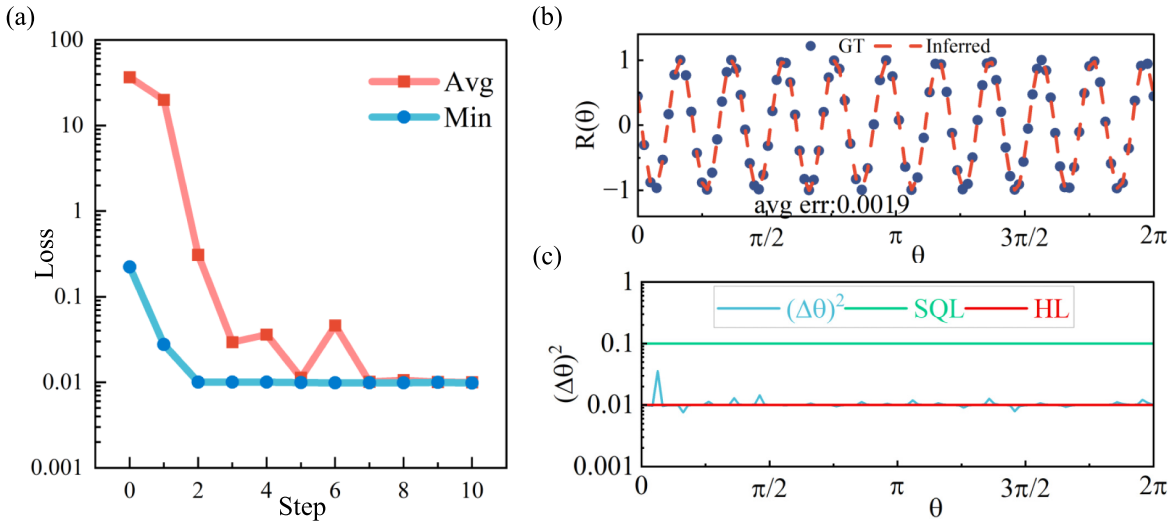

FIG. 16. (a) Illustration of the loss curve throughout the EA process, with the average loss across the population denoted by the red line and the minimum loss by the blue line. (b) Inferred response functions corresponding to the layout shown in Fig. 14(b) with the optimized observable being $O = \otimes_{i=1}^{10} U^*$. The dashed red line represents the exact response function (GT), while the points indicate the inferred response. (c) The estimated sensitivities related to the response function. The blue curve indicates the sensitivity level, while the green and red lines mark the SQL and HL, respectively.

satisfies that $a^2 + b^2 + c^2 = 1$. Given the Hermitian nature of Pauli matrices and their anticommutative properties, U is both Hermitian and unitary, allowing for the construction of the composite observable $O(\mathbf{x}) = \otimes_{i=1}^{N} U_i(\mathbf{x})$. With a fixed $\mathbf{x}$, we have the corresponding observable $O\mathbf{x}$ and the inferred trigonometric response function $R(\theta; \mathbf{x})$. Consequently, the sensitivity $(\Delta\theta)^2$ can be estimated by Eq. (19). Since the explicit coefficients of trigonometric polynomial are known, the empirical objective function

$$L(\mathbf{x}) = \mathbb{E}_\theta[(\Delta\theta)^2|\mathbf{x}] \tag{H1}$$

is numerically calculable, leading to the optimization problem

$$\min_{||\mathbf{x}||^2=1} L(\mathbf{x}). \tag{H2}$$

In our work, we consider an encoding Hamiltonian involving single-qubit interactions, specifically $H = \sum_i A_i$, where A_i represents the same single-qubit Hermitian operator acting on the ith qubit. The operator A can be expressed in its Bloch representation as $A = a_x X + a_y Y + a_z Z$, corresponding to a direction on the Bloch sphere.

When optimizing the observable O, we assume that the probe state takes the form $|\psi\rangle = |M\rangle^{\otimes n} + |m\rangle^{\otimes n}$, where $|M\rangle$ and $|m\rangle$ are the eigenstates of A. Under Hamiltonian evolution, a phase difference is introduced between these states, and the optimal strategy to detect this phase difference is to project onto the eigenbasis complementary to A.

Due to the symmetry of both H and $|\psi\rangle$, the measurement observable O is constructed as a product of single-qubit measurements $O = \bigotimes_i U_i$, where each $U_i = U$ represents a measurement axis orthogonal to A on the Bloch sphere. Thus, the measurement basis $U(\mathbf{x})$ described in this section can be represented as a single-qubit measurement aligned orthogonally to A.

This ensures that the measurement strategy is aligned with the encoding Hamiltonian, enabling us to approximately achieve the quantum Cramér-Rao bound (QCRB). The single-qubit measurement basis is sufficient in our scenario, given the nature of the single-qubit interactions in the Hamiltonian and the symmetry of the probe state and observable.

Considering the same task of 10-photon quantum sensing in the previous Appendix, we now use the EA to optimize the parameter $\mathbf{x}$. We define population of $\mathbf{x}$'s $D = 10$, the time step $T = 10$, and the selection factor $k = 3$. The probabilities for crossover and mutation are set to $p_c = 0.7$ and $p_m = 0.2$, respectively, with an individual mutation rate of $p_d = 0.2$. The blended-α crossover (BLX-α) [79] with $\alpha = 0.5$ and Gaussian mutation [77] methods are employed.

In Fig. 16(a), we show the curves of average loss of the population of $\mathbf{x}$'s and the minimum loss among them over steps. Figure 16(a) showcases the evolution of the average and minimum loss among the population across the steps. After 10 EA steps, we discerned an optimized $\mathbf{x}^* = (-0.6245, 0.7810, -0.0011)$ with the lowest loss, forming the optimized local observable U^*, leading to $O = \otimes_{i=1}^{10} U_i^*$. Notably, the influence of Pauli Z is very small. This result aligns with the fact that it is optimal to measure the probe state in Pauli X or Pauli Y when $H = \sum_{i=1}^{10} Z_i$ and the probe state previously prepared is a GHZ state. Figures 16(b) and 16(c) exhibit the inferred response function and the estimated sensitivity, respectively, with the optimized observable achieving the Heisenberg limit.

The method to optimize the operator O can readily fit into our DQS scheme as it does not use any information of the probe state or the Hamiltonian, thus satisfying environment agnostic. Since the optical setup is fixed and we only optimize the measurement observable, it does not cause much extra resource to previous steps of DQS.

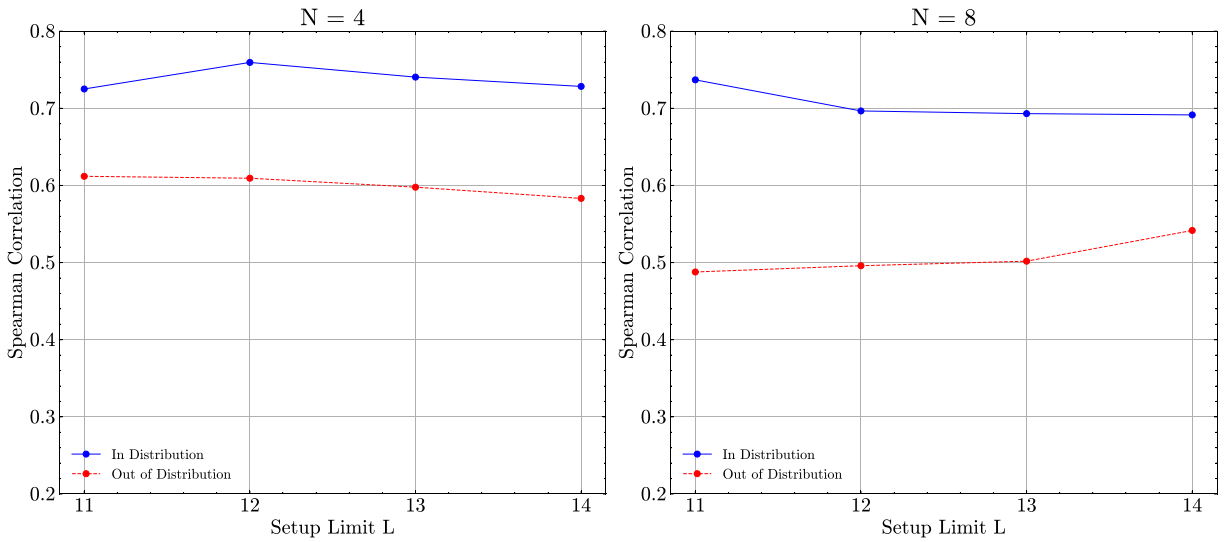

FIG. 17. Spearman correlation coefficient for test examples with $N = 4$ and 8. The blue line represents test examples whose lengths are within the limit L used during training (referred to as in distribution), while the red dashed line represents test examples with lengths exceeding L (referred to as out of distribution).

APPENDIX I: GENERALIZATION ABILITY OF THE GNN

To evaluate the generalization ability of the trained GNN, we extended our experiments to assess how well the model performs when the search space exceeds the training data set, particularly with larger optical setup lengths. Specifically, we varied the length limit L of the training examples, meaning that the optical setups in the training data set had lengths not exceeding L. The experiments were conducted with photon numbers $N = 4$ and 8, using a data set where optical setups ranged from 3 to 15 devices, consistent with the details provided in Sec. IV C of the main text. The training data set contained 50 000 examples, while the test data set contained 10 000 examples for both $N = 4$ and 8.

During training, we removed all examples with setup lengths greater than L. For testing, we split the test data set into two subsets: one containing setups with lengths no greater than L (referred to as in distribution, ID) and the other containing setups with lengths exceeding L (referred to as out of distribution, OOD). In Fig. 17, we present the Spearman correlation coefficient for models trained with $L = 11$, 12, 13, and 14. The results indicate a small gap between ID and OOD performance, while changes in L did not significantly affect this gap. This suggests that the observed gap is primarily due to the general challenge of out-of-distribution generalization in deep learning, which remains an open research question.

To further assess generalization beyond the training distribution, we tested the GNN model trained with $L = 11$ and $N = 8$ in a larger search space. It is important to note that the training data set did not include any setups with a quantum Fisher information (QFI) value of 64. For this experiment, we used the GNN along with an evolutionary algorithm (EA) as described in Appendix F. We started with 50 randomly initialized optical setups, with lengths ranging from $L_{\min}$ to $L_{\max}$, and refined them using 1000 iterations of EA. Table IV presents the results for different values of $L_{\min}$ and $L_{\max}$. Despite the initial search space being outside the training distribution, our method consistently found optimal candidates, demonstrating its generalizability. Interestingly, the GNN often identified setups with fewer devices than the initial configurations, suggesting that it learned meaningful patterns rather than simply memorizing, thereby avoiding unnecessary device usage.

APPENDIX J: ROBUSTNESS TO NOISY LABELS

To evaluate the robustness of our model against noisy labels, we conducted additional experiments where the training labels were subjected to different levels of noise. Specifically, we considered both four-photon and eight-photon tasks, using 50 000 training samples and 10 000 test samples for each setting, as described in the main text. The labels were estimated based on finite-fidelity quantum measurements such as swap test, with shot numbers set to 5000, 10 000, 50 000, and 100 000, respectively. These shot numbers introduce varying levels of statistical noise into the QFI labels, simulating the uncertainty that arises in practical quantum measurements.

TABLE IV. $L_{\min}$ and $L_{\max}$ refer to the initial minimum and maximum lengths when using the evolutionary algorithm (EA), while L refers to the length of the best final candidate found. "Y" indicates that the candidate is optimal; otherwise, "N" is shown. QFI represents the quantum Fisher information of the candidate.

No.	$L_{\min}$	$L_{\max}$	L	Is optimal	QFI
1	3	15	7	Y	64
2	11	11	10	Y	64
3	12	15	11	Y	64
4	15	20	16	Y	64
5	20	30	18	Y	64
6	3	30	6	Y	64

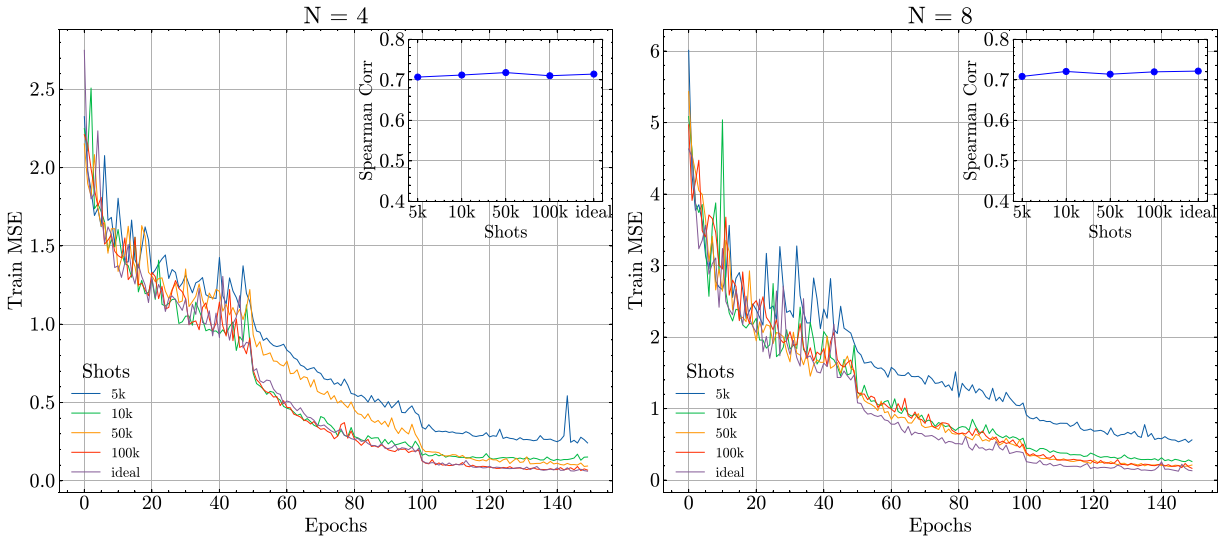

FIG. 18. Training loss of GNN models trained with noisy labels. The blue, green, yellow, and red lines represent the mean-squared error (MSE) during training for labels estimated from 5000, 10 000, 50 000, and 100 000 measurement shots, respectively, while the purple line corresponds to the noiseless ideal label. The inset shows the Spearman correlation coefficient for each GNN on the test set.

For comparison, we also included a GNN model trained on noiseless ideal labels as a baseline.

Figure 18 presents the training mean-squared error (MSE) over the first 150 epochs. We observed that models trained with noisier labels, such as those estimated from 5000 shots, exhibited slower convergence compared to those trained with labels from 100 000 shots. For instance, at the 100th epoch, the training loss for the model trained on labels with 5000 shots was approximately 0.2 higher for $N = 4$ and about 0.8 higher for $N = 8$, compared to the model trained with labels from 100 000 shots. This suggests that more accurate labels lead to faster training convergence.

However, as shown in the inset of Fig. 18, the Spearman correlation coefficient on the test set remains similar across models trained with different noise levels. These results demonstrate that while noisy labels can affect training convergence speed, the GNN model maintains robustness in the test phase, showing a similar performance regardless of the noise level in the training labels.

[1] V. Giovannetti, S. Lloyd, and L. Maccone, Advances in quantum metrology, Nat. Photon. **5**, 222 (2011).
[2] S. Pirandola, B. R. Bardhan, T. Gehring, C. Weedbrook, and S. Lloyd, Advances in photonic quantum sensing, Nat. Photon. **12**, 724 (2018).
[3] N. Aslam, H. Zhou, E. K. Urbach, M. J. Turner, R. L. Walsworth, M. D. Lukin, and H. Park, Quantum sensors for biomedical applications, Nat. Rev. Phys. **5**, 157 (2023).
[4] D. Feng, Review of quantum navigation, IOP Conf. Ser.: Earth and Environ. Sci. **237**, 032027 (2019).
[5] E. D. Caldwell, J.-D. Deschenes, J. Ellis, W. C. Swann, B. K. Stuhl, H. Bergeron, N. R. Newbury, and L. C. Sinclair, Quantum-limited optical time transfer for future geosynchronous links, Nature (London) **618**, 721 (2023).
[6] S. E. Crawford, R. A. Shugayev, H. P. Paudel, P. Lu, M. Syamlal, P. R. Ohodnicki, B. Chorpening, R. Gentry, and Y. Duan, Quantum sensing for energy applications: Review and perspective, Adv. Quantum Technol. **4**, 2100049 (2021).
[7] E. Polino, M. Valeri, N. Spagnolo, and F. Sciarrino, Photonic quantum metrology, AVS Quantum Sci. **2**, 024703 (2020).
[8] M. Barbieri, Optical quantum metrology, PRX Quantum **3**, 010202 (2022).
[9] J. Qin, Y.-H. Deng, H.-S. Zhong, L.-C. Peng, H. Su, Y.-H. Luo, J.-M. Xu, D. Wu, S.-Q. Gong, H.-L. Liu *et al.*, Unconditional and robust quantum metrological advantage beyond N00N states, Phys. Rev. Lett. **130**, 070801 (2023).
[10] A. Gu, L. Cincio, and P. J. Coles, Practical Hamiltonian learning with unitary dynamics and Gibbs states, Nat. Commun. **15**, 312 (2024).
[11] M. Fanizza, Y. Quek, and M. Rosati, Learning quantum processes without input control, PRX Quantum **5**, 020367 (2024).
[12] N. Thomas-Peter, B. J. Smith, A. Datta, L. Zhang, U. Dorner, and I. A. Walmsley, Real-world quantum sensors: Evaluating resources for precision measurement, Phys. Rev. Lett. **107**, 113603 (2011).
[13] K. Bongs, M. Holynski, J. Vovrosh, P. Bouyer, G. Condon, E. Rasel, C. Schubert, W. P. Schleich, and A. Roura, Taking atom interferometric quantum sensors from the laboratory to real-world applications, Nat. Rev. Phys. **1**, 731 (2019).
[14] J. Xavier, D. Yu, C. Jones, E. Zossimova, and F. Vollmer, Quantum nanophotonic and nanoplasmonic sensing: Towards quantum optical bioscience laboratories on chip, Nanophotonics **10**, 1387 (2021).

[15] M. Krenn, M. Malik, R. Fickler, R. Lapkiewicz, and A. Zeilinger, Automated search for new quantum experiments, Phys. Rev. Lett. **116**, 090405 (2016).

[16] P. Knott, A search algorithm for quantum state engineering and metrology, New J. Phys. **18**, 073033 (2016).

[17] L. O'Driscoll, R. Nichols, and P. A. Knott, A hybrid machine learning algorithm for designing quantum experiments, Quantum Mach. Intell. **1**, 5 (2019).

[18] R. Nichols, L. Mineh, J. Rubio, J. C. Matthews, and P. A. Knott, Designing quantum experiments with a genetic algorithm, Quantum Sci. Technol. **4**, 045012 (2019).

[19] A. Hentschel and B. C. Sanders, Efficient algorithm for optimizing adaptive quantum metrology processes, Phys. Rev. Lett. **107**, 233601 (2011).

[20] N. B. Lovett, C. Crosnier, M. Perarnau-Llobet, and B. C. Sanders, Differential evolution for many-particle adaptive quantum metrology, Phys. Rev. Lett. **110**, 220501 (2013).

[21] A. A. Melnikov, H. Poulsen Nautrup, M. Krenn, V. Dunjko, M. Tiersch, A. Zeilinger, and H. J. Briegel, Active learning machine learns to create new quantum experiments, Proc. Natl. Acad. Sci. USA **115**, 1221 (2018).

[22] H. Xu, J. Li, L. Liu, Y. Wang, H. Yuan, and X. Wang, Generalizable control for quantum parameter estimation through reinforcement learning, npj Quantum Inf. **5**, 82 (2019).

[23] X. Yang, J. Thompson, Z. Wu, M. Gu, X. Peng, and J. Du, Probe optimization for quantum metrology via closed-loop learning control, npj Quantum Inf. **6**, 62 (2020).

[24] F. Belliardo, F. Zoratti, and V. Giovannetti, Applications of model-aware reinforcement learning in Bayesian quantum metrology, Phys. Rev. A **109**, 062609 (2024).

[25] B. Koczor, S. Endo, T. Jones, Y. Matsuzaki, and S. C. Benjamin, Variational-state quantum metrology, New J. Phys. **22**, 083038 (2020).

[26] J. J. Meyer, J. Borregaard, and J. Eisert, A variational toolbox for quantum multi-parameter estimation, npj Quantum Inf. **7**, 89 (2021).

[27] M. Krenn, J. S. Kottmann, N. Tischler, and A. Aspuru-Guzik, Conceptual understanding through efficient automated design of quantum optical experiments, Phys. Rev. X **11**, 031044 (2021).

[28] C. Ruiz-Gonzalez, S. Arlt, J. Petermann, S. Sayyad, T. Jaouni, E. Karimi, N. Tischler, X. Gu, and M. Krenn, Digital discovery of 100 diverse quantum experiments with pytheus, Quantum **7**, 1204 (2023).

[29] V. Gebhart, R. Santagati, A. A. Gentile, E. M. Gauger, D. Craig, N. Ares, L. Banchi, F. Marquardt, L. Pezzè, and C. Bonato, Learning quantum systems, Nat. Rev. Phys. **5**, 141 (2023).

[30] G. Torlai, G. Mazzola, J. Carrasquilla, M. Troyer, R. Melko, and G. Carleo, Neural-network quantum state tomography, Nat. Phys. **14**, 447 (2018).

[31] J. Carrasquilla, G. Torlai, R. G. Melko, and L. Aolita, Reconstructing quantum states with generative models, Nat. Mach. Intell. **1**, 155 (2019).

[32] A. M. Palmieri, E. Kovlakov, F. Bianchi, D. Yudin, S. Straupe, J. D. Biamonte, and S. Kulik, Experimental neural network enhanced quantum tomography, npj Quantum Inf. **6**, 20 (2020).

[33] S. Ahmed, C. Sanchez Muñoz, F. Nori, and A. F. Kockum, Quantum state tomography with conditional generative adversarial networks, Phys. Rev. Lett. **127**, 140502 (2021).

[34] J. Gao, L.-F. Qiao, Z.-Q. Jiao, Y.-C. Ma, C.-Q. Hu, R.-J. Ren, A.-L. Yang, H. Tang, M.-H. Yung, and X.-M. Jin, Experimental machine learning of quantum states, Phys. Rev. Lett. **120**, 240501 (2018).

[35] X.-F. Yin, Y. Du, Y.-Y. Fei, R. Zhang, L.-Z. Liu, Y. Mao, T. Liu, M.-H. Hsieh, L. Li, N.-L. Liu *et al.*, Efficient bipartite entanglement detection scheme with a quantum adversarial solver, Phys. Rev. Lett. **128**, 110501 (2022).

[36] D. Koutný, L. Ginés, M. Moczała-Dusanowska, S. Höfling, C. Schneider, A. Predojević, and M. Ježek, Deep learning of quantum entanglement from incomplete measurements, Sci. Adv. **9**, eadd7131 (2023).

[37] X. Zhang, M. Luo, Z. Wen, Q. Feng, S. Pang, W. Luo, and X. Zhou, Direct fidelity estimation of quantum states using machine learning, Phys. Rev. Lett. **127**, 130503 (2021).

[38] Y.-D. Wu, Y. Zhu, G. Bai, Y. Wang, and G. Chiribella, Quantum similarity testing with convolutional neural networks, Phys. Rev. Lett. **130**, 210601 (2023).

[39] Y. Qian, Y. Du, Z. He, M. hsiu Hsieh, and D. Tao, Multimodal deep representation learning for quantum cross-platform verification, Phys. Rev. Lett. **133**, 130601 (2024).

[40] Y. Zhu, Y.-D. Wu, G. Bai, D.-S. Wang, Y. Wang, and G. Chiribella, Flexible learning of quantum states with generative query neural networks, Nat. Commun. **13**, 6222 (2022).

[41] D. Flam-Shepherd, T. C. Wu, X. Gu, A. Cervera-Lierta, M. Krenn, and A. Aspuru-Guzik, Learning interpretable representations of entanglement in quantum optics experiments using deep generative models, Nat. Mach. Intell. **4**, 544 (2022).

[42] T. Jaouni, S. Arlt, C. Ruiz-Gonzalez, E. Karimi, X. Gu, and M. Krenn, Deep quantum graph dreaming: Deciphering neural network insights into quantum experiments, Mach. Learning Sci. Technol. **5**, 015029 (2024).

[43] Z. He, M. Deng, S. Zheng, L. Li, and H. Situ, Training-free quantum architecture search, in *Proceedings of the AAAI Conference on Artificial Intelligence* (AAAI, Washington, DC, 2024), Vol. 38, pp. 12430–12438.

[44] C. Lei, Y. Du, P. Mi, J. Yu, and T. Liu, Neural auto-designer for enhanced quantum kernels, in *The Twelfth International Conference on Learning Representations* (ICLR, Appleton, WI, 2024).

[45] R. A. Fisher, On the mathematical foundations of theoretical statistics, Philos. Trans. R. Soc. London, Ser. A **222**, 309 (1922).

[46] C. R. Rao, Information and the accuracy attainable in the estimation of statistical parameters, in *Breakthroughs in Statistics: Foundations and Basic Theory* (Springer, Berlin, 1992), pp. 235–247.

[47] S. L. Braunstein and C. M. Caves, Statistical distance and the geometry of quantum states, Phys. Rev. Lett. **72**, 3439 (1994).

[48] Y.-F. Huang, B.-H. Liu, L. Peng, Y.-H. Li, L. Li, C.-F. Li, and G.-C. Guo, Experimental generation of an eight-photon Greenberger–Horne–Zeilinger state, Nat. Commun. **2**, 546 (2011).

[49] X.-L. Wang, L.-K. Chen, W. Li, H.-L. Huang, C. Liu, C. Chen, Y.-H. Luo, Z.-E. Su, D. Wu, Z.-D. Li *et al.*, Experimental ten-photon entanglement, Phys. Rev. Lett. **117**, 210502 (2016).

[50] M. Malik, M. Erhard, M. Huber, M. Krenn, R. Fickler, and A. Zeilinger, Multi-photon entanglement in high dimensions, Nat. Photon. **10**, 248 (2016).

[51] J. Liu, H. Yuan, X.-M. Lu, and X. Wang, Quantum fisher information matrix and multiparameter estimation, J. Phys. A: Math. Theor. **53**, 023001 (2020).

[52] M. Cerezo, A. Arrasmith, R. Babbush, S. C. Benjamin, S. Endo, K. Fujii, J. R. McClean, K. Mitarai, X. Yuan, L. Cincio *et al.*, Variational quantum algorithms, Nat. Rev. Phys. **3**, 625 (2021).

[53] M. Cerezo, A. Sone, J. L. Beckey, and P. J. Coles, Sub-quantum fisher information, Quantum Sci. Technol. **6**, 035008 (2021).

[54] J. L. Beckey, M. Cerezo, A. Sone, and P. J. Coles, Variational quantum algorithm for estimating the quantum fisher information, Phys. Rev. Res. **4**, 013083 (2022).

[55] Y. Shi, Z. Huang, S. Feng, H. Zhong, W. Wang, and Y. Sun, Masked label prediction: Unified message passing model for semi-supervised classification, in *Proceedings of the Thirtieth International Joint Conference on Artificial Intelligence, IJCAI-21*, edited by Zhi-Hua Zhou (International Joint Conferences on Artificial Intelligence Organization, 2021), pp. 1548–1554.

[56] C. Huerta Alderete, M. H. Gordon, F. Sauvage, A. Sone, A. T. Sornborger, P. J. Coles, and M. Cerezo, Inference-based quantum sensing, Phys. Rev. Lett. **129**, 190501 (2022).

[57] M. Fey and J. E. Lenssen, Fast graph representation learning with pytorch geometric, *ICLR Workshop on Representation Learning on Graphs and Manifolds* (2019).

[58] D. P. Kingma and J. Ba, Adam: A method for stochastic optimization, in *International Conference on Learning Representations (ICLR)* (San Diega, CA, USA, 2015).

[59] A. Paszke, S. Gross, F. Massa, A. Lerer, J. Bradbury, G. Chanan, T. Killeen, Z. Lin, N. Gimelshein, L. Antiga *et al.*, Pytorch: An imperative style, high-performance deep learning library, in *Proceedings of the 33rd International Conference on Neural Information Processing Systems* (Curran Associates Inc., Red Hook, NY, USA, 2019).

[60] X. Gu, Melvin: Automated search for new quantum experiments – python version, https://github.com/XuemeiGu/MelvinPython.

[61] M. Krenn, M. Erhard, and A. Zeilinger, Computer-inspired quantum experiments, Nat. Rev. Phys. **2**, 649 (2020).

[62] L. Van der Maaten and G. Hinton, Visualizing data using t-SNE, J. Mach. Learning Res. **9**, 2579 (2008).

[63] C. Bonato, M. S. Blok, H. T. Dinani, D. W. Berry, M. L. Markham, D. J. Twitchen, and R. Hanson, Optimized quantum sensing with a single electron spin using real-time adaptive measurements, Nat. Nanotechnol. **11**, 247 (2016).

[64] C. D. Marciniak, T. Feldker, I. Pogorelov, R. Kaubruegger, D. V. Vasilyev, R. van Bijnen, P. Schindler, P. Zoller, R. Blatt, and T. Monz, Optimal metrology with programmable quantum sensors, Nature (London) **603**, 604 (2022).

[65] R. Demkowicz-Dobrzański, W. Górecki, and M. Guţă, Multi-parameter estimation beyond quantum fisher information, J. Phys. A: Math. Theor. **53**, 363001 (2020).

[66] M. Yu, D. Li, J. Wang, Y. Chu, P. Yang, M. Gong, N. Goldman, and J. Cai, Experimental estimation of the quantum fisher information from randomized measurements, Phys. Rev. Res. **3**, 043122 (2021).

[67] A. Rath, C. Branciard, A. Minguzzi, and B. Vermersch, Quantum fisher information from randomized measurements, Phys. Rev. Lett. **127**, 260501 (2021).

[68] J. Gacon, C. Zoufal, G. Carleo, and S. Woerner, Simultaneous perturbation stochastic approximation of the quantum fisher information, Quantum **5**, 567 (2021).

[69] S. Aaronson, Shadow tomography of quantum states, in *Proceedings of the 50th Annual ACM SIGACT Symposium on Theory of Computing* (Association for Computing Machinery, New York, 2018), pp. 325–338.

[70] H.-Y. Huang, R. Kueng, and J. Preskill, Predicting many properties of a quantum system from very few measurements, Nat. Phys. **16**, 1050 (2020).

[71] Y. Du, Y. Yang, T. Liu, Z. Lin, B. Ghanem, and D. Tao, Shadownet for data-centric quantum system learning, arXiv:2308.11290.

[72] D. Hendrycks and K. Gimpel, Gaussian error linear units (GELUs), arXiv:1606.08415.

[73] https://github.com/ZeddTheGoat/Deep-learning-Quantum-Sensing.

[74] S. Boixo, S. T. Flammia, C. M. Caves, and J. M. Geremia, Generalized limits for single-parameter quantum estimation, Phys. Rev. Lett. **98**, 090401 (2007).

[75] M. Napolitano, M. Koschorreck, B. Dubost, N. Behbood, R. Sewell, and M. W. Mitchell, Interaction-based quantum metrology showing scaling beyond the Heisenberg limit, Nature (London) **471**, 486 (2011).

[76] P. Yin, X. Zhao, Y. Yang, Y. Guo, W.-H. Zhang, G.-C. Li, Y.-J. Han, B.-H. Liu, J.-S. Xu, G. Chiribella *et al.*, Experimental super-Heisenberg quantum metrology with indefinite gate order, Nat. Phys. **19**, 1122 (2023).

[77] T. Bäck, D. B. Fogel, and Z. Michalewicz, *Handbook of evolutionary computation* (IOP Publishing Ltd., GBR, 1997).

[78] F.-A. Fortin, F.-M. De Rainville, M.-A. Gardner, M. Parizeau, and C. Gagné, DEAP: Evolutionary algorithms made easy, J. Mach. Learning Res. **13**, 2171 (2012).

[79] L. J. Eshelman and J. D. Schaffer, Real-coded genetic algorithms and interval-schemata, in *Foundations of Genetic Algorithms* (Elsevier, Amsterdam, 1993), Vol. 2, pp. 187–202.